719936

ORNL-4007
UC-41 – Health and Safety

Contract No. W-7405-eng-26

HEALTH PHYSICS DIVISION ANNUAL PROGRESS REPORT

For Period Ending July 31, 1966

K. Z. Morgan, Director
W. S. Snyder, Assistant Director
E. G. Struxness, Assistant Director

REPOSITORY NMES/KYO/Vault
COLLECTION Central Files
BOX No. ORNL-4007
FOLDER

OCTOBER 1966

OAK RIDGE NATIONAL LABORATORY
Oak Ridge, Tennessee
operated by
UNION CARBIDE CORPORATION
for the
U. S. ATOMIC ENERGY COMMISSION

1147698

A-00385
Human Studies Project

Contents

SUMMARY ix

PART I. RADIOACTIVE WASTE DISPOSAL

1. FATE OF NUCLIDES IN TERRESTRIAL ENVIRONMENT 3
   - Field Plot Studies 3
   - Cobalt Sorption by Pulverized Minerals and Clays 7
2. DISPOSAL BY HYDRAULIC FRACTURING 10
   - Rock Mechanics 10
   - Mix Development 12
3. DISPOSAL IN NATURAL SALT FORMATIONS 15
   - Preparation for Project Salt Vault 15
   - Startup of Project Salt Vault 17
   - Preliminary Results in Project Salt Vault 18
   - First Fuel Assembly Changeout 23
   - Pillar Model Studies 23
   - Disposal of High-Level Waste in Selected Rock Formations 26
4. APPLICATION OF MINERAL EXCHANGE TO REACTOR TECHNOLOGY 27
   - Disposal of Gases into Permeable Formations 27
   - Nonequilibrium Ion Exchange 30
   - Hydroxide Consumption by Conasauga Shale 31
   - Behavior of Curium in Mineral Exchange Systems 31
   - Interpretation of Cation Exchange by Alumina 32
5. ENGINEERING, ECONOMIC, AND SAFETY EVALUATIONS 34
   - Clinch River Safety Analyses 34
   - ^{85}Kr and Tritium in an Expanding World Nuclear Power Industry 35
   - Long-Range Waste Management Study 37
6. RELATED COOPERATIVE PROJECTS 40
   - Cooperation of Other Agencies in ORNL Studies 40
   - Special Project 40
   - Visiting Investigators from Abroad 40
   - Visiting Investigator Abroad 40
   - Nuclear Safety Review 40
   - *Health Physics* Journal 40

1147699

Committee Work 40
Participation in Educational Programs 41
Nuclear Safety Information Center 41

PART II. RADIATION ECOLOGY

7. RESPONSES OF ANIMAL POPULATIONS TO IONIZING RADIATION 45
Radiation Sensitivity in Indigenous Small Mammals 45
Incorporation of a Thymidine Analog into Indigenous Rodents 47
Radiation Effects on Carp Reproduction 48
Population Genetics and Radiation Effects Studies 48

8. RESPONSES OF PLANTS TO IONIZING RADIATION 51
Growth and Mortality Responses of Conifers to Fast-Neutron Irradiation 51
Radiation Dose to Roots of Potted Plants from Reactor Fast Neutrons and Soil Activation Products 52
Mineral Uptake Mechanism Affected by Fast-Neutron Radiation 53
Effects of Fast-Neutron Radiation on Physiological Processes 53
Environmental and Genetic Modifications of Radiosensitivity 55
Structural Changes in Irradiated Plants 56

9. RADIONUCLIDE CYCLING IN TERRESTRIAL ECOSYSTEMS 58
Trends of ^{137}Cs in the *Liriodendron* Forest Vegetation 58
Foliage Biomass and Primary Productivity in the ^{137}Cs-Tagged *Liriodendron* Forest 58
^{137}Cs Distribution in Canopy Food Chains of the *Liriodendron* Forest 60
Equilibration of ^{137}Cs Body Burdens in Forest Myriapoda 63
^{134}Cs Turnover by Isopods Under Natural and Laboratory Conditions 65
Relationship Between Metabolism and ^{134}Cs Turnover by Forest Isopods 67
Isotopic Determination of Food Consumption and Utilization by Isopods 68
Trophic Efficiencies of Insect Herbivory Using ^{86}Rb and ^{32}P Tracers 70
Efficiency of Radioisotope Transfer in Predator-Prey Systems 71
^{106}Ru Elimination by Brown Crickets (*Acheta domesticus*) 72
Losses of ^{137}Cs and ^{60}Co from Leaf Litter 73
^{137}Cs Transfer in Terrestrial Microcosms 73
Accumulation and Production in a Pioneer Ecosystem of Kudzu Vine at Copperhill, Tennessee 73
Movement of ^{137}Cs in Pine Forest Floor Subsystems 74
Soil Studies in Herbaceous Ecosystems 74
Possible Mechanisms of Cobalt Sorption on Soil Clays 77
Precision and Accuracy of Basal Cover Estimates 78
Value of a Vacuum Clipper in Harvesting Herbage 81
Electronic Data Processing of Floristic Records 82
Forest Management 82

1147700

10. RADIONUCLIDE CYCLING IN AQUATIC ECOSYSTEMS 84
Cesium and Potassium in White Crappie and Other Clinch River Fish 84
Feeding Rate of Carp in White Oak Lake 87
Effect of Trophic Level on Radionuclide Accumulation by Fish 88
Radionuclides in Periphyton 88
Use of Artificial Substrata to Estimate the Productivity of Periphyton 90
Estimate of Periphyton Mass and Stream Bottom Area Using ^{32}P 90
Primary Productivity Measurement 92
Trace Elements in Plankton 93
Trace Elements in Seston 98
Transfer of ^{137}Cs, ^{106}Ru, and ^{60}Co Between Detritus and Benthic Macroinvertebrates in Microcosms 100
Accumulation of ^{32}P by Biota and Their Substrates in a Tagged Stream 101
11. THEORETICAL AND SYSTEMS ECOLOGY 102
A Systems Philosophy 102
Mathematical Modeling of Natural Populations 103
Ecosystem Maintenance and Transformation Models as Markov Processes with Absorbing Barriers 104
Model Simulation of Oak Ridge Vegetation Succession 106
Kinetics of ^{134}Cs in Terrestrial Microcosms 107
Nonlinear Programming in Ecology 109
Computer Programs for Ecological Problems 110
Productivity of a Planktonic Diatom Determined from Data on Mixed Species Populations 113
Growth Models for Plants 114
The Optimum Site Problem 117
Year-to-Year Prediction of ^{137}Cs Movement in the Tagged Forest 119

PART III. RADIATION PHYSICS

12. THEORETICAL RADIATION PHYSICS 123
High-Energy Dosimetry 123
General Concepts in Radiation Dosimetry 123
The Static Dielectric Constant of a Free-Electron Gas 124
The Screening Constant of an Electron Gas 125
Positron Annihilation in Metals 125
Positron Effective Mass in a Free-Electron Gas 126
Electron Mean Free Paths in a Free-Electron Gas 127
The Penetration of Low-Energy Electrons in Condensed Matter 127
Coupled Electron-Hole Cascade in a Free-Electron Gas 128
Photoelectric Emission from Thin Foils 128
The Excitation of Surface Plasmons by Photons 128
Double Plasmon Excitation by Charged Particles 129

1147701

13. ATOMIC AND MOLECULAR RADIATION PHYSICS 130
Alpha-Particle Ionization of Binary Gas Mixtures 130
Electron Impact Excitation of Atoms and Molecules Using a Low-Energy Electron Scavenger Technique 131
Finite-Medium Effects in Irradiated Gases 133
Time-of-Flight Determinations of Electron Diffusion Coefficients and Electron Drift Velocities in Ethylene, Water Vapor, and Hydrogen 133
Effects of Experimental Boundaries on the Measurement of Diffusion Coefficients and Drift Velocities in Swarm Methods 134
Electron Time-of-Flight Studies Using Electron Multiplier Techniques 134
Effect of Capture and Loss Processes on Time Distributions of Diffusing Electrons 135
Swarm Determination of the Cross Section for Momentum Transfer in Ethylene and in Ethylene Mixtures 136
Studies of Electronic Bound States in the Field of a Permanent Electric Dipole 137
Analysis of Electron Swarm Data to Obtain Transport Cross Sections 137
Swarm-Beam Studies of Polyatomic Molecules 138
Lifetimes of Temporary Negative Ions 140
Studies of Dissociative Electron Attachment in H_2O and D_2O 141
Interaction of Low-Energy Electrons with Atomic Oxygen 142
Potential Energy Curves for Diatomic Molecules 144
Molecular Orbitals of Magnesium Porphin 144
Approximate Representation of the Hartree-Fock Equations Through a Pseudopotential 144

14. INTERACTION OF RADIATION WITH LIQUIDS AND SOLIDS 147
Transition Radiation Due to Nonnormally Incident Electrons 147
Transition Radiation and Bremsstrahlung from Ag and Al Foils Bombarded by Nonnormal Incidence Electrons 148
Reflectance of Evaporated Aluminum Films in the Wavelength Region 800 to 2000 A 150
Optical and Photoelectric Properties of Evaporated Ag and Al Films 151
Optical and Electronic Properties of Tin 153
Optical and Electronic Properties of Sodium in the Wavelength Region 420 to 2000 A 155
Electron Slowing-Down Spectra in Aluminum 157

15. PROFESSIONAL HEALTH PHYSICS TRAINING 161

16. PHYSICS OF TISSUE DAMAGE 164
Excimer-Scintillator Investigations 164
Radiation Interactions with Liquids 166
Optical Properties of Polystyrene 167
Electronically Excited Amino Acids 168
Low-Energy Electron Transmission in Solids 168

1147702

PART IV. RADIATION DOSIMETRY

17. ICHIBAN STUDIES 173
Ichiban Liaison 173

18. SPECTROMETRY AND DOSIMETRY RESEARCH 175
An Absolute Neutron Dosimeter Based on a Generalized Concept for Radiation Dosimetry 175
Prediction of Biological Damage from Stopping-Power Theory 179
Transistorized Fast-Neutron Integrator – Radsan Mark II 182
Production of Gamma Rays by Neutrons in Air 183
Neutron Cross Sections for the Elements in Tissue 186
Ionization Recombination Studies 186

19. DOSIMETRY APPLICATIONS 189
Metaphosphate Glass Dosimetry 189
A Neutron-Energy Threshold Detector System Employing Solid-State Nuclear Track Detectors 190
Nuclear Accident Dosimeter Intercomparison Study 192
Depth-Dose Studies 195
Experimental Depth-Dose Studies in Water Phantoms 196
Sensitivity of Cellulose Acetate Butyrate for Alpha-Particle Track Registration 198
Irradiation of Plastics in DOSAR Low-Energy Accelerator 200
Radsan Correction-Factor Studies 203

20. SPECIAL PROJECTS AND HPRR OPERATIONS 205
Operation HENRE Accelerator 205
DOSAR Low-Energy Accelerator 207
Health Physics Research Reactor 209

PART V. INTERNAL DOSIMETRY

21. INTERNAL DOSE ESTIMATION 213
Revision of Standard Man 213
The Estimation of Exposure to an Aerosol Based on a Revised Standard Lung Model 216
Variation of Dose Delivered by ^{137}Cs as a Function of Body Size from Infancy to Adulthood 221
Iodine Retention 228
Computer Studies of Linear Combination of Exponentials Representing Power Functions 232

22. STABLE ELEMENT METABOLISM 237
Tissue Analysis Laboratory 237
Inorganic Composition of Ashed Biological Materials 237
Elemental Composition of Standard Man 240

1147703

PART VI. HEALTH PHYSICS TECHNOLOGY

23. AEROSOL PHYSICS 245
Adhesion of Solid Particles to Solid Surfaces 245
Survey of Adventitious Electrical Fields in the Working Environment 250
Studies of Surface Contamination 251
Environmental Studies 254
Empirical Dose Model for Reactor Debris Particles 256
Dosimetry of Small Particles 257

24. APPLIED INTERNAL DOSIMETRY 260
ORNL In Vivo Gamma-Ray Spectrometry Facility 260
In Vivo Detection and Measurement of ^{90}Sr-^{90}Y Internal Contamination 261
Computer Analysis of Whole-Body Count Data 261
Correction of ^{239}Pu-^{241}Am Wound Count for Attenuation in Tissue and for Different Ratios of ^{241}Am to ^{239}Pu 264
Absorption of ^{90}Sr from a Puncture Wound 266
Preventing Radiostrontium Loss in the Precipitation of Alkaline-Earth Phosphates from Urine with NH_4OH 267

THESES, PAPERS, PUBLICATIONS, AND LECTURES

THESES 271
PAPERS 271
PUBLICATIONS 277
LECTURES 287

1147704

Summary

PART I. RADIOACTIVE WASTE DISPOSAL

1. Fate of Nuclides in Terrestrial Environment

Continuing studies of the field plots show a reduced rate of loss of ^{137}Cs in the fall and winter months of the second year. There is a logarithmic relationship between ^{137}Cs loss and the soil loss. Mass balance analyses do not provide a satisfactory accounting of the total ^{137}Cs applied to the clipped meadow plot.

Studies of the selective adsorption of cobalt by layer lattice silicates show that adsorption is influenced by the method of sample preparation. With identical sample preparation techniques, trioctahedral lattices sorb more cobalt than comparable minerals with dioctahedral lattices.

2. Disposal by Hydraulic Fracturing

The most probable failure mechanisms limiting the ultimate capacity of the shale formation in the hydraulic-fracturing waste-disposal method appear to be related to the stresses induced in the rocks surrounding the injection by the injection itself. The problem of defining the number and size of injections required to produce a failure condition is under investigation using elastic analysis.

Examination of the nuclide retention properties of the set grouts, especially those containing low-cost fly ash, continued.

3. Disposal in Natural Salt Formations

Final preparations for Project Salt Vault were completed during the first half of fiscal year 1966. In addition to experimental equipment, a hoist and ventilation fan were installed at the waste shaft. Prior to startup of the experiment, a number of preoperational tests were conducted using both empty fuel assembly canisters and canisters loaded with 500 curies of ^{60}Co. A number of minor modifications to both the equipment and the handling procedures were made as a result of these tests.

On November 15, 1965, operation of Project Salt Vault was commenced. By November 19, seven canisters, containing 14 ETR fuel assemblies and a total of 1,000,000 curies, had been lowered into the mine and installed in hole liners in the floor of the newly mined areas. The demonstration is proceeding without difficulty. Preliminary results indicate that the rapidity of the transference of thermally induced stresses from the floor, through the supporting pillars, and into the roof is the only effect so far which was not anticipated.

On June 13–16, 1966, an additional set of fuel assemblies were placed in the mine. Roof bolts have been installed to strengthen the roof in the experimental area. Pillar model studies have shown that shale partings at the floor or roof allow an accelerated rate of deformation of the pillars.

4. Application of Mineral Exchange to Reactor Technology

In the event of a nuclear incident involving fuel element meltdown, ^{131}I appears to present the most serious short-term hazard. If the radioactive gases could be pumped underground, the delay time afforded by adsorption and by physical movement through the porous medium and dilution would cause a reduction in the relative hazard by a few orders of magnitude. Strontium-90 would present the most serious potential for contaminating groundwater near the site of discharge.

1147705

Laboratory studies conducted on the sorption of iodine by clays suggest that the iodine consists of condensed I_2 and chemisorbed I_2. Samples leached with water retain a finite quantity of I_2, also suggesting a fixed capacity for the chemisorption of iodine.

A computer program has been written to describe the transient behavior of radionuclides in the ground when the transporting solution is of a different concentration than the original groundwater. Experimental data, obtained on a Berea sandstone for different sets of conditions, confirm the suitability of Glueckauf's model for the passage of a wide band of solute through a chromatographic column, modified for changes in the adsorptive capacity due to changes in the total electrolyte concentration and for nonequilibrium sorption conditions.

Preliminary data on curium behavior suggest that mechanisms other than ion exchange may play dominant roles in its behavior in the ground.

5. Engineering, Economic, and Safety Evaluations

An age-dependent metabolic model was used to estimate dose equivalents received by the skeleton from ingestion of Clinch River water. For the age groups considered, this model gave an average dose 15% larger than the adjusted ICRP model. The dose rate associated with buildup of ^{85}Kr in the atmosphere and ^{3}H in the atmosphere and circulating water was estimated for an expanding free-world nuclear power economy. For complete releases to year 2000, the estimated whole-body dose rate from ^{85}Kr was 1.8 millirems/year in the first $\frac{1}{4}$ mile of the atmosphere and the body tissue dose rate from ^{3}H was 7.2×10^{-4} millirem/year by inhalation and 1.4×10^{-3} millirem/year by ingestion of water. A long-range waste management study was initiated.

6. Related Cooperative Projects

Other agencies continued to participate in our studies. Three alien guests were in residence during the year. One staff member was assigned to work in Belgium and France. Members of the section participated in Project Arkose of the Department of Defense, ASCE Committee on Sanitary Engineering Aspects of Nuclear Energy, and NAS-NRC Committee on Pollution.

One member has also served as assistant news editor for the United States for *Health Physics* and as an assistant editor of *Nuclear Safety*. Two members of the section taught a course at the University of Tennessee, and a series of lectures have been given to the U.S. Public Health Service.

PART II. RADIATION ECOLOGY

7. Responses of Animal Populations to Ionizing Radiation

Six species of rodents in the family Cricetidae, two species in the Muridae, and two species of shrews in the family Soricidae were irradiated at seven dose levels ranging from 500 to 2000 rads. Estimates of LD_{50-30} ranged from 535 to 1050 rads. The most radioresistant and most radiosensitive species were both in the Cricetidae.

The thymidine analog 5-^{131}iodo-2′-deoxyuridine can be used as an index of radiation damage, cell proliferation rates, and general metabolism in free-ranging native rodents. Acute radiation doses of 100, 500, and 1000 rads depressed whole-body incorporation of this antimetabolite in cotton rats to 76, 38, and 28%, respectively, of controls, and activity levels in the radiosensitive intestines were reduced to 47, 18, and 1.5% respectively. Rate of cell proliferation was related to the general metabolism of the three species tested.

Study of the natural population of *Chironomus tentans* in White Oak Lake and White Oak Creek has continued since the preliminary investigations in 1960. Two hundred larvae of another species of *Chironomus* belonging to the *plumosus* group were collected from White Oak Lake and analyzed for chromosomal aberrations. In contrast to *C. tentans*, which is chromosomal polymorphic, previous examinations of this species from nonirradiated populations revealed no endemic inversions; and the species is considered to be chromosomal monomorphic in this area. One aberration, a small inversion, was found in the larvae from the irradiated population. This finding agrees with previous conclusions based on our studies with *C. tentans*, that ionizing radiation from the contaminated environment increased the frequency of new chromosomal aberrations, but that these new aberrations were eliminated rapidly by natural selection.

1147706

8. Responses of Plants to Ionizing Radiation

Two species of pine, white pine (*Pinus strobus* L.) and shortleaf pine (*Pinus echinata* Mill.), were exposed to four levels of fast-neutron radiation (75, 100, 150, and 200 rads – tissue dose in air) at the DOSAR facility. Growth inhibitions occurred in all radiation treatment groups and reached maxima about two months following irradiation. Needle mortality of old leaves appeared in the 150- and 200-rad treatments within two to four weeks following irradiation. Over winter, plants in the 75- and 100-rad treatment groups exhibited 100% needle mortality. Under the greenhouse conditions in this study the minimum lethal dose (LD_{100}) was 75 rads for all plants.

A study was conducted to determine the neutron dose distribution and additional gamma and beta dose delivered to plant roots by activation products in the potting soil used for plant irradiation studies at the DOSAR facility. The experimental packages were exposed 1.0 m from the reactor core to 2056 rads (tissue dose in air) of fast neutrons delivered over a 10-min period. The major activation products were ^{56}Mn, ^{51}Cr, ^{86}Rb, ^{181}Hf, and ^{95}Zr-^{95}Nb in decreasing order of abundance. Manganese constituted 96% of the measured activity from activation products.

The effects of fast-neutron radiation on the growth and uptake of ^{65}Zn were studied in three-year-old red oak (*Quercus rubra* L.) seedlings. Potted seedlings received shoot irradiations of 505 and 1011 rads (tissue dose in air) delivered over a period of 8 min. Primary and secondary stem growth, root growth, and new leaf development were inhibited. An initial stimulation of ^{65}Zn uptake was observed following irradiation but disappeared by about 20 days. Retardation of uptake was found about ten weeks following exposure of seedlings to the higher dose.

In studies of the predictability of the interphase nuclear volume technique for radiation sensitivity it was found that plants growing under field conditions were found to suffer severe growth inhibitions at gamma radiation exposures two to three times less than those necessary to produce the same effect on plants in growth chambers with optimized environmental conditions. Experimental stress conditions, particularly moisture stress, given postirradiation lowered exposure requirements even more. Under growth chamber conditions, fast-neutron exposures were an order of magnitude less than the gamma exposures necessary to produce severe growth inhibition or death. Seasonal changes in nuclear volume of 14 plant species suggest that radiosensitivity would change by a factor of 1.5 to 3.0 during the year for dormant vs actively growing plants.

9. Radionuclide Cycling in Terrestrial Ecosystems

Year-to-year changes in distribution of ^{137}Cs in the tagged *Liriodendron* forest have been measured and accounted for in terms of major above- and below-ground transfers of ^{137}Cs. Concentrations in the forest canopy decreased each year since 1962. Annual transfers out of the canopy decreased accordingly from 1962 through 1965. Production and energy studies in the forest showed that annual production was 554 leaves/m^2. In caloric terms annual net foliage production by all tree species in the tagged forest was calculated to be 1.55×10^3 kcal/m^2.

Cesium-137 concentrations in the sessile canopy arthropods were greatest in leaf-eating herbivores and were least in sap-feeding herbivores. Food chain analyses showed a general decrease in ^{137}Cs concentrations during movement along food chains, with herbivorous insects (except for sap feeders) having the highest concentrations, omnivores intermediate concentrations, and predators the lowest concentrations per unit weight.

Radiotracer tags of ^{86}Rb and ^{32}P of plants growing in the field were used to measure food consumption and the efficiencies of trophic transfer for beetle populations under natural environmental conditions. Consumption of vegetation by beetles averaged 15.9 mg/day or (56.8 ± 1.40)% of their dry body weight. The respective turnover times for these food constituents were ^{86}Rb, 1.44 days; dry matter, 3.66 days; energy (calories), 4.42 days.

A comparison of ^{106}Ru and ^{137}Cs elimination by the brown cricket (*Acheta domesticus*) showed similar biological half-lives for the longer components of cesium and ruthenium elimination. Radiocesium was found in the muscle, fat body, and other soft tissues, whereas ^{106}Ru concentrated mainly in the intestinal walls and was not detected in the fat body. Neither radionuclide accumulated in the integument.

A mathematical interpolation scheme of contour mapping was used to develop maps of soil prop-

1147707

erties. To test the validity of a "limited field–computer mapping" approach, the study area was first surveyed by conventional techniques. Then elevations were taken on a 50 × 50 ft grid and used as inputs for a computer program which produced contour maps with a Calcomp plotter.

10. Radionuclide Cycling in Aquatic Ecosystems

Studies of cesium and potassium concentrations in the white crappie (*Pomoxis annularis*) showed that potassium concentrations in the flesh were relatively constant throughout the year, whereas stable cesium concentrations varied by a factor of 2. The period of low cesium concentration did not coincide completely with a reduced summer feeding activity by fish. In other Clinch River species potassium also was relatively constant, whereas cesium concentrations differed by a factor of 4. Bluegills and channel catfish had the lowest cesium concentrations, white bass and white crappie had the highest concentration, and freshwater drum had intermediate concentrations. There was no concise relationship between trophic position of the fish and their cesium content, although white bass and white crappie, the most piscivorous species, also had the highest cesium concentrations.

An investigation of fish in White Oak Lake to determine if the trophic position of the fish was correlated with its concentration of a radionuclide yielded negative results. Five species were analyzed for ^{137}Cs, ^{60}Co, and ^{90}Sr. The species, in order of increasing relative trophic position, were carp, gizzard shad, bullhead, bluegill, and largemouth bass.

A technique for using ^{32}P to indirectly measure periphyton mass and stream bottom area was developed and used successfully on a small stream. Three standard methods of measuring aquatic primary productivity, pH, ^{14}C, and O_2 evolution, were compared in seven 48-hr experiments performed in situ in Melton Hill Lake. The methods yielded different results. Based on similar results in other experiments with a variety of planktonic material, it was concluded that productivity values obtained by indirect procedures applied under field conditions are a function primarily of the measurement method. Differences between methods were both quantitative and qualitative.

11. Theoretical and Systems Ecology

A survey was made of literature from ecology, natural resource management, systems analysis, and operations research in order to better define the area of work called systems ecology. Ecological compartment models were treated as Markov processes with absorbing barriers to simulate succession of vegetation on the Oak Ridge Reservation. The study of radiocesium kinetics in microecosystems consisting of different combinations of tagged white oak leaf litter, soil microflora, millipedes, and aqueous leachate was completed. Turnover data indicate (1) that identical compartments turned over radiocesium at variable rates in the different microcosms and (2) that turnover rates of compartments increased with greater system complexity. The results showed that material transfers in connected systems are influenced by the organizational networks which define interactions between component parts. Consequently, network characteristics should be regarded as significant ecological variables in studies of energy and material movements, including transfers of radioactive substances.

Several growth models for plants were investigated for their predictive value. Equations were developed to show the residual influence of the nitrogen and phosphorus on height growth.

PART III. RADIATION PHYSICS

12. Theoretical Radiation Physics

Work in theoretical radiation dosimetry has included the calculation of dose due to protons and neutrons having energies up to 400 Mev for a cylindrical tissue phantom with elliptical cross section. This work is being extended to the Bev region using simplified models for the interaction processes. Further research into general concepts in radiation dosimetry has been carried out. Quantum mechanical collision theory has been applied in an attempt to elucidate those physical characteristics of radiation and its interaction with matter that are most relevant in producing biological responses.

Theoretical work in the area of solid-state plasma physics has involved a large number of related topics. Monte Carlo techniques have been ap-

1147708

plied to the determination of the static dielectric constant of the electron gas, which in turn has been employed in the calculation of the annihilation rates of thermalized positrons in electron gases of various densities. These rates are in good agreement with experimental data in free-electron-like metals. Using many-body perturbation theory, the contribution to the effective mass of a thermalized positron in a free-electron-like metal due to Coulomb interaction with conduction electrons has been evaluated. This contribution is found to amount to about 10% of the electron mass in an electron gas at a density corresponding to the conduction band in metallic Na.

The mean free path of hot electrons in a free-electron gas is of great interest in connection with recent experimental work done in this Division and elsewhere. Calculations of this quantity from a Bethe-Goldstone equation for the scattering of a hot electron from a particular electron in the Fermi gas are being carried out. This calculation accounts for both the operation of the exclusion principle in intermediate states and for dielectric screening by the electron gas. A Monte Carlo calculation of low-energy electron penetration in thin metal foils has been compared with experimental results of Nakai and Birkhoff, yielding fair agreement. An analytical approximation to the low-energy end of the electron-hole cascade spectrum in an electron gas has been found. This solution predicts an inverse fourth-power dependence of the flux of electrons or holes upon energy measured from the top of the conduction band.

A study of the theoretical photoelectron yield from thin metal foils by photons incident such that the electric vector has a nonzero component normal to the foil surface has shown that a peak should exist at the volume plasma frequency. In addition, it is found that the yield at this frequency should fluctuate as the foil thickness is varied. The probability of surface plasmon excitation by photons incident upon a thick metal foil has been found to increase linearly above the threshold energy. The phenomenon of two-plasmon excitation in characteristic energy loss experiments is being investigated theoretically. This process may be important at low electron energies, where the first Born approximation becomes suspect.

13. Atomic and Molecular Radiation Physics

Studies of the ionization produced by alpha particles in gas mixtures have been extended to cases involving at least one noble gas. The data yield empirical parameters which may be interpreted as describing the partitioning of dose between the components. Kinetic interpretation of the ensuing Hornbeck-Molnar processes may then be made. A novel technique has been developed for investigating inelastic scattering mechanisms of electrons. At the threshold for each new transition the scattered electron is left with approximately zero energy and may thus be scavenged and detected as SF_6^-. A computational investigation of the diffusion of ions to a boundary in irradiated gases has been completed and suggests that thermal convection currents are responsible for much of the wall neutralization inferred from chemical yields.

The time-of-flight technique for measuring the transport properties of electrons in gases has been given a more reliable foundation. Errors arising from experimental boundaries, counter dead time, and instrumental fluctuations are either negligible or may be removed at the data-treatment stage. Diffusion coefficients thus obtained in several gases and mixtures are often in marked disagreement with results from the Townsend-Huxley method; occasional deviations from the Nernst-Einstein relation have also been noted. An expression has been derived that shows the effect of temporary electron capture on diffusion coefficients. This mechanism may be partially responsible for the above discrepancies.

Electron drift velocity measurements continue to provide information on momentum transfer cross sections. Temperature effects in pure ethylene suggest, surprisingly, that it has a velocity-independent cross section. The cross sections previously found for polar molecules in an ethylene medium remain anomalously large. Temporary electron capture by an electric dipole is being investigated as a source of these anomalies. Finally, improved analytical techniques have been devised for extracting electron transport cross sections in the rare gases from the macroscopic transport properties.

Electron beam and swarm techniques have been successfully combined to yield the mechanism and energy-resolved cross sections for electron

1147709

attachment by large organic molecules. Dissociative capture occurs for all halogenated benzene compounds, although the nitro derivatives of benzene may also capture thermal electrons nondissociatively. The lifetimes of these long-lived parent molecule ions with respect to autoionization can be measured in the time-of-flight mass spectrometer. With the measured cross sections and lifetimes, one may calculate the density of negative ion states from detailed balance. Comparison with thermodynamic estimates of these level densities then yields lower limits to molecular electron affinities. The swarm-beam combination is being extended to study the dissociative attachment of simple molecules (e.g., H_2O and D_2O) to obtain information concerning the primary interactions responsible for electron capture. Hartree-Fock calculations have been completed on still another mechanism of electron capture – the radiative attachment to oxygen atoms.

Calculations of potential energy curves of diatomic molecules are being continued. The Rydberg-Klein method is used to analyze spectroscopic data. The molecular orbitals of magnesium porphin, a chlorophyll constituent, are being classified as a means of interpreting the electronic absorption spectrum of this molecule. A tractable formalism for coping with Hartree-Fock calculations is being developed and applied to systems of large atomic number.

14. Interaction of Radiation with Liquids and Solids

The vacuum ultraviolet spectra of light emitted by electron-beam-bombarded metal films gives much detailed information about the electronic transitions taking place. Recently a German laboratory has found that Ag targets bombarded with electrons not entering normal to the surface emit a monochromatic component at the surface plasmon wavelength, and they have attributed this to surface plasmon decay, although there were strong theoretical arguments that such decay should be radiationless. A theoretical and experimental program at ORNL has corroborated their experimental findings for Ag and found a similar peak in Al. Studies of polarization and of dependence on electron energy, film thickness, and electron incidence angle show, however, that the light is bremsstrahlung rather than surface plasmon radiation. Interesting optical interference effects are found in thin Al films both theoretically and in the laboratory.

Optical studies in the vacuum ultraviolet were carried out for Al, Ag, Sn, and Na. The Al data were taken under ultrahigh vacuum conditions ($\sim 10^{-8}$ torr) but still required correction for surface oxidation. Reflectances were free-electron-like down to 790 A and showed a small absorption at 1250 A attributed to surface plasmon excitation. Also, photoelectric studies showed a large decrease in yield of photoelectrons beyond the threshold photon energy for surface plasmon excitation. This absorption of photoelectrons is thought to be similar to the absorption phenomena noted in electron transmission experiments described in "Physics of Tissue Damage," Chap. 16, this report. Reflectivity studies on Ag and Sn helped separate free-electron and interband components in the dielectric constants. Interference studies in Na between 420 and 2000 A, the region of transparency, were successful in determining the index of refraction and setting an upper limit to the extinction coefficient. Here also interband contributions to the dielectric constant were measured.

Electron slowing-down spectra were obtained in Al, a more nearly tissue-equivalent medium than those studied heretofore. Alloys of radioactive Cu, Au, or Pd ($\sim$1% by weight) in Al yielded absolute spectra in reasonable agreement with the Spencer-Attix theory above 10 kev, but these spectra were more than an order of magnitude higher than theory at low energies. LET spectra derived from the data and theoretical stopping powers substantiate the assumption usually made in radiobiology that the electron spectrum in a beta-irradiated medium is mono-LET in character.

15. Professional Health Physics Training

The Health Physics Training Program included 16 fellowship students from Vanderbilt University and the University of Tennessee who reported to ORNL for summer on-the-job instruction in applied and research health physics. Division personnel visited 33 colleges and universities to give seminars on various research problems of current interest and also to recruit qualified students into the program. The Health Physics Di-

1147710

vision provided research facilities and advisors for 22 graduate students who were conducting thesis research. Teaching assistance was given to the University of Tennessee for its program in Radiation Physics and to Vanderbilt University for its course in Radiation Physics. Numerous short courses and lectures were presented for other groups and agencies.

16. Physics of Tissue Damage

Several liquid organic scintillators have been developed which utilize excimer formation to enhance the fluorescent efficiency. Although the primary purpose of the studies is to understand energy absorption and transfer in these liquids, the enhanced light emission, exceeding the best liquid scintillators by at least a factor of 3, promises to have important uses in many practical applications. Equipment to measure the optical constants of liquid water in the vacuum ultraviolet has been designed, constructed, and tested. Such optical data can be used to determine which electronic levels are excited in liquid water by ionizing radiation. Techniques developed may be applied to body fluids and to photochemical studies on liquids in the vacuum ultraviolet, where no work has previously been reported. Optical studies on solid polystyrene in the same spectral region have revealed resonance absorptions at 6.5 and 19.2 ev, which are attributed to π-electron excitation and a collective resonance involving all 40 noncore electrons respectively.

Preliminary studies on electron-bombarded aromatic amino acids show unusually large transmissions through layers 200 to 600 A thick. These observations are not understood at present but may make easier the ultimate purpose of the research, namely, the observation of fluorescence and phosphorescence of these films with the hope of obtaining information about initial excitation and subsequent events. Electron transmission of metallic films a few hundred angstroms in thickness was measured for Al, Mg, Tl, In, and Cu. Monoenergetic electrons between 3 ev and 3 kev were found to excite surface and volume plasmons and ionize inner electron shells with probabilities varying with electron energy. A Monte Carlo calculation for aluminum showed substantial agreement with transmission data for this metal. A sharp minimum in absorption was found for In and Mg just above the threshold for surface plasmon excitation.

PART IV. RADIATION DOSIMETRY

17. Ichiban Studies

The major efforts in the Ichiban studies were directed to liaison, depth-dose studies, and the shielding problems associated with heavily shielded survivors. During the visits to Japan detailed descriptions for computing final dose values, based on the new air-dose curves and shielding equations, were written and discussed with the shielding technicians.

18. Spectrometry and Dosimetry Research

Research in spectrometry and dosimetry was directed, in the main, to the spectrometry of indirectly ionizing radiations and to the calculation and measurement of energy loss functions for protons and heavy ions in tissue. Other studies included cross-section and reaction-product compilations for tissue, nuclear accident detector research, and advances in instrumentation.

19. Dosimetry Applications

There were several significant developments in dosimetry applications including: (1) improvements in the techniques of dosimetry with threshold detectors; (2) improvements in photoluminescent detectors; (3) development of methods and techniques for using insulating solids as track detectors for heavy ions; and (4) development of a convenient system for applying correction factors to pulse integrator responses.

20. Special Projects and HPRR Operations

The final testing of the HENRE accelerator was completed at ORNL, and the machine was shipped to Nevada and installed on the BREN tower. A low-energy accelerator was placed in service at the DOSAR facility and is being used extensively in the research program. The Health Physics Research Reactor has continued as a versatile irradiation facility for health physics and radiobiological research for ORNL and non-ORNL programs.

1147711

PART V. INTERNAL DOSIMETRY

21. Internal Dose Estimation

Revision of Standard Man

For approximately 17 years standard man has been a hypothetical adult man whose weight was 70 kg and who has been described by a limited amount of data. Due to the increased need for additional information, standard man is now being revised. This study represents the first attempt, as far as is determined by the authors, to define in detail a 70-kg man. A table of organ weights is included, and in some cases where the weights present a special problem, a short description also is included as to the basis for these weights.

The Estimation of Exposure to an Aerosol Based on a Revised Standard Lung Model

The Report of the ICRP Task Group on Lung Dynamics is the result of an intensive review of the literature on the subject. The lung model defined by this report is considerably more detailed than previous models and provides estimates of deposition and retention of an aerosol in each of three subregions of the lung. The report does not discuss the estimation of dose to these regions. In this study masses are assigned to the nasopharyngeal region (N-P), the tracheobronchial region (T-B), and the pulmonary region (P), which the report defines. Also, the question of the effective energy to be used for each of these regions is considered. Because of the unusual geometrical shapes of these regions, the estimates given here are not firm, and the difficulties are discussed.

Variation of Dose Delivered by ^{137}Cs as a Function of Body Size from Infancy to Adulthood

Six phantoms approximating the body size and shape of humans from birth to adulthood were mathematically constructed. A Monte-Carlo-type code was used to compute the gamma dose rate in about a hundred subregions of each phantom from a ^{137}Cs source uniformly distributed in a phantom. The distributions of gamma dose rate throughout the phantoms and the dose rate variation with phantom size or age were determined.

Iodine Retention

Using transfer coefficients for the normal individual, the differential equations for a three-compartmental model for iodine retention by the body are solved. The equilibrium iodine concentration in the body for a constant intake of iodine, as well as the total dose from a single intake of radioiodine, is expressed as a rational function of the transfer coefficients.

Computer Studies of Linear Combinations of Exponentials Representing Power Functions

It is found that the finite sum of N exponentials

$$\sum_{i=1}^{N} \alpha_i^{-n} e^{-\alpha_i t}$$

will generally approximate the power function

$$\frac{\Gamma(1-n)}{\Delta\alpha} t^{-(1-n)}$$

over a finite time period for cases in which $n \leq 0.333$ and $\alpha_i = \alpha_1 + (i-1)\Delta\alpha$. Graphs showing the comparison between the exponential sum and the power function are presented.

22. Stable Element Metabolism

Tissue Analysis Laboratory

In the tissue analysis program, laboratory techniques have been extended to include methods for determining cesium and rubidium in teen-age diet samples.

Inorganic Composition of Ashed Biological Materials

In a separate study, laboratory methods have been developed for determining the anionic composition for diets and excreta from a balance study on two individuals.

1147712

Elemental Composition of Standard Man

Using the previous data obtained from this study and data from many different sources, the amounts of 38 elements in the total body of a 70-kg man have been calculated.

PART VI. HEALTH PHYSICS TECHNOLOGY

23. Aerosol Physics

Adhesion of solid particles to solid surfaces is being studied theoretically and experimentally. Since capillary and electrical forces predominate, emphasis is placed on these phenomena. A physical model is suggested to predict the magnitude of the capillary force between a glass particle and a glass surface. Experimental data confirm a predicted aging effect and the maximum expected force at 100% relative humidity; however, deviations from the simple model at lower relative humidity appear to be in contradiction with the Gibbs-Thomson relation concerning the vapor pressure over a curved surface. An empirical equation relating the electrical repulsion of a conductive spherical particle in contact with a charged conductive surface is derived from experimental data and is seen to agree approximately with theoretical calculations for a flat flake.

A survey of two local hot-cell facilities shows the existence of electrically charged surfaces which are of sufficient magnitude to enhance local deposition of airborne particles. All hot-cell and strip-chart recorder windows were charged, as were all floor tiles (vinyl asbestos) and sponge rubber floor mats; about half of the glass windows in partitions and doors were charged. The observed surface charges were all negative.

Studies of surface contamination measurement and resuspension potential have been continued using CuO dust in a room (8 × 12 × 8 ft) simulating a small laboratory of average cleanliness. This work has shown that the resuspension potential of a given contaminant can be assessed almost independently of surface composition – dry hard, dry dusty, dry porous, sticky, oily – on the basis of measurements made with a resuspension sampler (SMAIR) developed by this group. It is seen also that particles larger than about 2 μ in diameter are more readily resuspended than are smaller particles. The resuspension studies (bench-top scale) have been extended to liquid spills. A cupric nitrate deposit left on a stainless steel surface after drying of a liquid spill could not be resuspended by the action of air jets, although the smear test removed 80% of the deposited copper.

Deposition and retention of simulated radioactive particles on the skin is being studied using fluorescent wax spheres (50 μ to 1 mm diameter), and carbon-coated depleted uranium dicarbide spheres (230 μ diameter). Initial sticking amounted to about 55% for small wax spheres (104 to 125 μ diameter) and from 6 to 44% for larger wax spheres (297 to 500 μ diameter) on moderately dry skin but approached 100% on skin wet with perspiration. The relatively heavier UC_2 spheres were retained about the same length of time or somewhat longer than wax spheres of the same size. Decontamination tests using wax spheres (100 μ to 1 mm diameter) show that, except for very small particles (1 to 2 μ diameter), essentially complete decontamination is effected by simple actions such as brushing the arm, rinsing with water, or washing with soap and water.

Dosimetry of small radioactive particles in contact with the skin or the lining of the gastrointestinal tract is complicated by the fact that some of the particles may differ significantly from the composition of tissue. An empirical model is suggested whereby a library of beta-gamma energy spectra and the associated tissue depth dose data for certain specified geometries may be used to approximate the depth dose from an unknown source so long as the source spectrum is known. At present the library includes ^{45}Ca and ^{89}Sr in 1-cm-diam graphite spheres containing 17 wt % of uranium.

The principle of extrapolation dosimetry is being applied to determining the skin and gastrointestinal tract dose from small (~100-μ-diam) irradiated reactor fuel particles as a function of decay time. The anthracene extrapolation dosimeter, described in the annual report for last year, has been modified to include NE 102-A plastic scintillators in a variety of sizes from 11 mm diameter × 500 μ thick to 1 mm diameter × 5 μ thick. An example of dose measurement using an extrapolation ion chamber and the extrapolation scintillator is given for UC_2 fuel beads irradiated for 10 min and observed at decay times from 30 min to two days. The combination of the two extrapolation dosimeters provides a useful range extending over six orders of magnitude in dose rate.

1147713

Part V. Internal Dosimetry

W. S. Snyder

1147715

24. Applied Internal Dosimetry

During the period July 1965 through May 1966 a total of 628 whole-body counts were made on 463 persons. Approximately 89% of the persons counted showed a normal human gamma-ray spectrum. Two employees, exposed to ^{90}Sr-^{90}Y ($SrTiO_3$) in January 1964, have been recounted at approximately one-month intervals for 849 days; the half-time for lung clearance appears to be in excess of 1000 days. Both routine and special whole-body gamma-ray spectra are now analyzed by a new computer program, ALPHA, which provides a wide selection of options including least-squares estimates of up to 20 radionuclides in each spectrum, automatic compensation for gain and threshold shifts, and an indication of "suspicious" channels where peaks may exist in the data but are not requested in the analysis.

Although most internal exposures examined by the Applied Internal Dosimetry group arise as a result of inhalation, the next most significant mode of intake results from wounds sustained on contaminated objects. An empirical approach is outlined for estimating the ratio of ^{241}Am to ^{239}Pu in an exposure mixture, and, using these data along with thin-crystal-probe absorption measurements on the wound, a method is given for estimating the quantities of ^{241}Am and of ^{239}Pu and the approximate depth of the deposit. An accidental exposure to ^{90}Sr-^{90}Y occurred when an employee received a puncture wound with a contaminated wire which penetrated four layers of gloves. The ^{90}Y content of the finger was determined by beta-absorption counting and has been followed for five months: absorption of ^{90}Sr into the bloodstream (~88% in <2 months) was estimated by urinalysis and analysis of blood samples; after the first two months the half-life for strontium elimination appears to be $\geq$500 days. An improved urinalysis procedure providing for efficient recovery of strontium and of various transuranic elements is shown to yield a constant recovery (95.0% $\pm$ 0.3) of strontium from urine samples ranging in volume from 500 to 1500 ml: essentially, this is a variation of the alkaline-earth phosphate precipitation, in which the key factors are the addition of excess calcium (60 mg per 500 ml of urine), excess H_3PO_4 (to give 0.1 *M*), excess NH_4OH (to give pH 9), and the exclusion of atmospheric CO_2 from the sample.

1147714

21. Internal Dose Estimation

W. S. Snyder
S. R. Bernard
Monica Boyd[1]
Mary Jane Cook
Wallace Davis III[1]
C. F. Holoway
H. L. Fisher, Jr.[2]
Mary R. Ford
Isabel H. Tipton[3]

REVISION OF STANDARD MAN

W. S. Snyder Mary Jane Cook
Isabel H. Tipton

Although standard man, as a typical radiation worker, was established approximately 17 years ago, there has been no systematic revision of the concept since that time, nor has it been extended to include other members of the population. Standard man should include the information needed for estimation of dose, whether from external or from internal sources; it should provide an estimate of the variability of dose due to individual differences and should offer methods of adjusting the estimate to correct for an individual's characteristics.

The original standard man was formalized by the International Commission on Radiological Protection (ICRP) at a conference at Chalk River in 1949.[4] This first standard man consisted of little more than (1) the specifications of the weights of some of the important organs and tissues, (2) specifications of intakes of air, water, and a few elements, and (3) some data on excretion. With increasing use of internally and externally applied radiation, it has become a necessity to expand the concept of standard man and to reevaluate the existing parameters.

The ICRP has organized a Task Group for the Revision of Standard Man, and the authors of this report are members of this group. Although the final values of the organ and tissue weights given here are the responsibility of the authors and not listed as representing the views of the task group, nevertheless, the authors are glad to acknowledge the very considerable influence of the other members of the task group on the work reported here. These members are Dr. L. Karhausen (Euratom) and Dr. G. Parry-Howells (United Kingdom Medical Research Council). The contribution of Dr. E. S. Nasset (formerly of the University of Rochester) should be acknowledged also. In particular, Dr. Karhausen has gathered and evaluated much of the data which are reported here in only slightly modified form in some cases. The authors have attempted to deal with the tissues and organs which present special problems either because little or no data were available or because of wide discrepancies of reported values. Each of these cases is discussed briefly below.

When data are selected or interpreted to define a typical or standard adult, it is necessary to have in mind the type of individual to be defined. Many of the data reported on organ weights or masses of tissues were not obtained from bodies of persons of the desired type. For example, age and weight of the subject may be expected to vary widely for much of the data, and in many cases it is necessary to scale the results to correct for this. A compilation of data without regard to the different characteristics of many of the subjects might give

[1]Summer employee.

[2]U.S. Public Health Service.

[3]Physics Department, University of Tennessee.

[4]Chalk River Conference on Permissible Internal Dose, a conference of representatives from the United Kingdom, Canada, and the United States, held in Chalk River, Canada, September 29–30, 1949, RM-10, 1950.

1147716

erroneous ideas of the interrelations of the organs and tissues of the body.

The organ weights of the hypothetical individual defined here are given in Table 21.1. This individual is considered to be a radiation worker who weighs 70 kg (~154.3 lb), is 174 cm (69.1 in.) tall, and is between 20 and 30 years of age. The values selected for the organ weights are taken from many sources and have been adjusted in some cases to correspond to an adult of the above weight, height, and age. Included with the weight of each organ or tissue given in Table 21.1 are the nerves, fascia, blood vessels, and lymphatic tissue such as lymph nodes within the tissue, blood and other fluids which would not be lost when the organ or tissue sample was removed during a postmortem examination, and other connective tissue except tendons and ligaments; tendons and ligaments are considered separately.

Gastrointestinal Tract (GI)

The values for the GI tract are based on the report prepared for ICRP Committee II by Eve.[5]

Lungs

The data are from the ICRP Committee II Task Group on Lung Dynamics.[6]

Skeleton[7-13]

Due to the presence of bone marrow, fat, and water, the weight of the skeleton was one of the most difficult to select. Many investigators have studied only dry, defatted bone or bones rather than the whole skeleton. Because it is so difficult to obtain an entire skeleton by dissection, data on the skeleton as a whole are not plentiful. The estimated total wet skeletal weight of 9400 g given here is intended to include bone marrow but includes neither cartilage nor dense connective tissue which may be cut away.

Adipose Tissue[14-16]

The term "adipose tissue" is used to represent (1) the subcutaneous tissue, which is a patent, fatty tissue underneath the skin, and (2) "other," which includes such fatty tissues as omentum and that which surrounds the individual organs. The term "fat" is restricted to the chemical constituent of all tissues which may be extracted with ether or other organic solvents.

Adipose tissue is one of the most widely variable tissues in weight and proportion since it is the chief factor in obesity. Standard man is assumed to be a well-developed, but nonobese, male by the criteria set by Morse and Soeldner,[15] who reported a value of 18.9% of total body weight for the adipose tissue of a group of healthy male subjects whose average weights and heights are close to those of standard man.

Aorta

Because the aorta is really external to both the heart and the lungs, it is the only blood vessel whose weight has not been considered to be included in that of the organ or tissue with which it is closely associated in the body.

Blood[7,17,18]

Although the total blood in the body of standard man has a weight of 5512 g (volume = 5200 ml),

[5] I. S. Eve, *Health Phys.* 12, 131 (1966).

[6] Task Group on Lung Dynamics, *Health Phys.* 12, 173 (1966).

[7] R. P. Custer, *An Atlas of the Blood and Bone Marrow*, Saunders, Philadelphia. 1949.

[8] R. E. Ellis, *Phys. Med. Biol.* 5, 255 (1961).

[9] G. Hudson, *Nature* 205, 96 (1965).

[10] M. W. Ingalls, *Am. J. Anat.* 48, 45 (1931).

[11] A. L. Merz *et al.*, *Am. J. Phys. Anthropol.* 14, 589 (1956).

[12] M. Trotter and R. P. Peterson, *J. Bone Joint Surg.* 44-A, 669 (1962).

[13] H. Q. Woodard and E. Holodny, *Phys. Med. Biol.* 5, 57 (1960).

[14] J. Brozek (ed.), *Ann. N. Y. Acad. Sci.* 110, 1–101 (1963).

[15] W. I. Morse and J. S. Soeldner, *Metabolism* 12, 9 (1963).

[16] J. P. Schaeffer (ed.), *Morris' Human Anatomy*, McGraw-Hill, New York, 1953.

[17] R. H. Altman, *Blood and Other Body Fluids*, Fed. Am. Soc. Exptl. Biol., Washington, 1961.

[18] M. J. Yiengst and N. W. Shock, *J. Appl. Physiol.* 17, 195 (1962).

1147717

Table 21.1. Organs and Tissues of Standard Man

	Mass (g)	Percent of Total Body
Adipose tissue	13,000	18.6
Subcutaneous	[9,500][a]	[13.6][a]
Other	[3,500]	[5.0]
Adrenals (2)	14	0.020
Aorta	100	0.14
Blood - total	[5,512] (5200 ml)	[7.9]
Blood vessels (including pulmonary)		
Contents (blood)	2,862 (2700 ml)	4.1
Brain	1,400	2.0
Cartilage and dense connective tissue	4,000	5.7
Eyes (2)	15	0.021
Fluids, miscellaneous	385	0.55
Gall bladder	10	0.014
GI tract	2,000	2.9
Esophagus	[50]	[0.071]
Stomach	[150]	[0.21]
Intestine	[1,800]	[2.57]
Contents of GI tract	1,005	1.4
Hair	15	0.021
Heart	350	0.50
Contents (blood)	318 (300 ml)	0.45
Kidneys (2)	310	0.44
Larynx	15	0.021
Liver	1,800	2.6
Lungs (2)	1,000	1.4
Muscle	27,000	38.6
Nails	10	0.014
Pancreas	90	0.13
Parathyroid (4)	0.2	0.0003
Pineal	0.2	0.0003
Pituitary	0.6	0.0006
Prostate	16	0.023
Salivary Glands (6)	85	0.12
Skeleton	9,400	13.4
Bone	[6,400]	[9.1]
Red marrow	[1,300]	[1.9]
Yellow marrow	[1,700]	[2.4]
Skin	4,000	5.7
Spinal cord	28	0.040
Contents (cerebrospinal fluid)	221 (220 ml)	0.32
Spleen	175	0.25
Teeth	46	0.066
Testes (2)	60	0.086
Thymus	20	0.029
Thyroid	16	0.023
Tongue	50	0.071
Tonsils (2)	3	0.0043
Trachea	15	0.021
Ureters (2)	16	0.023
Urinary bladder	45	0.064
Contents (urine)	102 (100 ml)	0.15
Urethra	2	0.0029
Total body	70,000	

[a]Numbers in brackets not included in totals.

1147718

part of this blood is included in the weights of organs and tissues. Only that blood which can be considered to be flowing in the large blood vessels and thus lost when the organs are removed for weighing during a postmortem examination is included as a separate item, "Contents of Blood Vessels." The remaining blood which would not drain from the organ is termed "trapped blood." The amount of trapped blood has been estimated in all organs except liver, muscle, spleen, and skeleton on the basis of the quantity of iron found in each organ by spectrographic analysis.[19] If we assume 5×10^{-4} g of Fe per milliliter of blood[20] and all of the Fe in the organs except those named specifically above occurred in the trapped blood, the quantity of trapped blood may be calculated by dividing the number of grams of iron in a tissue by 5×10^{-4}. The amount of blood in liver, spleen, and bone was calculated assuming 80% of the iron found in the hemopoietic system to be stored and 20% to be associated with trapped blood.[21] The amount in muscle was estimated, taking into consideration the relative quantities of myoglobin and hemoglobin in muscle.[22,23] Thus, the circulating blood represents the difference between total and trapped blood.

Cartilage and Dense Connective Tissue

We tentatively suggest a value of 4000 g as the weight of cartilage and dense connective tissue. This value was estimated in two ways. (1) Collagen accounts for about one-third of the proteins in the body.[24,25] For soft tissues the words "connective tissue" have been assumed to be synonymous with "collagen," and the amount has been calculated as one-third of the crude protein content of a tissue. By studying drawings of muscle and skeleton in *Gray's Anatomy*[26] and *Morris' Anatomy*[16] which were made carefully to scale, the amount of cartilage and dense connective tissue was estimated to be 4600 g. (2) The suggested organ weights for standard man were totaled (omitting cartilage and dense connective tissue) and the sum subtracted from 70 kg. The difference indicated that approximately 4000 g should be allocated for cartilage and dense connective tissue.

Fluids, Miscellaneous

This heading includes synovial fluid and any other fluids, excluding blood, which might be lost when an organ is dissected for weighing.

Many of the weights in Table 21.1 are tentative and in no way should they be considered final. This study does represent the first attempt so far as we can determine to define a 70-kg man in such detail.

THE ESTIMATION OF EXPOSURE TO AN AEROSOL BASED ON A REVISED STANDARD LUNG MODEL

Mary R. Ford W. S. Snyder

The lung model used by ICRP to estimate values of $(MPC)_a$[27,28] was revised recently by a task group created to advise ICRP Committee II concerning lung dynamics. The report of the task group[29] specifies a more realistic and quantitative scheme for the deposition and clearance of particulate matter from the respiratory tract than did the previous model. It does not, however, discuss the actual computation of dose to the various compartments of the lung or to the lung as a whole. Additional information needed for the estimation of dose to various portions of the lung is discussed here, and methods of obtaining the dose estimates are presented.

---

[19] I. H. Tipton and M. J. Cook, *Health Phys.* 9, 103 (1963).

[20] P. B. Hawk *et al.*, *Practical Physiological Chemistry*, 12th ed., Blakiston, Philadelphia, 1947.

[21] C. V. Moore and R. Dubach, "Iron," in *Mineral Metabolism*, vol. 2, part B, ed. by C. L. Comar and F. Bronner, Academic, New York, 1962.

[22] B. A. Houssay *et al.*, *Human Physiology*, 2d ed., McGraw-Hill, New York, 1955.

[23] E. L. Smith, "Cobalt," in *Mineral Metabolism*, vol. 2, part B, ed. by C. L. Comar and F. Bronner, Academic, New York, 1962.

[24] I. S. Kleiner and J. M. Orten, *Biochemistry*, 6th ed., Mosby, St. Louis, 1962.

[25] J. Gross, *Sci. Am.* **204**, 120 (1961).

[26] C. M. Goss (ed.), *Gray's Anatomy of the Human Body*, 27th ed., Lea and Febiger, Philadelphia, 1959.

[27] *Report of Committee II on Permissible Dose for Internal Radiation*, ICRP Publication 2, Pergamon, London, 1959.

[28] J. N. Stannard, "An Evaluation of Inhalation Hazards in the Nuclear Energy Industry," p. 306 in *Peaceful Uses of Atomic Energy*, vol. 23, 1958.

[29] P. E. Morrow, Chairman, Task Group on Lung Dynamics, *Health Phys.* 12, 173 (1966).

1147719

The model respiratory tract, as described by the task group, consists of three compartments: the nasopharynx (N-P), beginning with the anterior nares and extending back and down to the level of the larynx; the trachea and bronchial tree (T-B), including the terminal bronchioles; and the pulmonary (P) compartment. The schematic portrayal of these compartments, together with the associated deposition and clearance processes as shown in the report[29] of the task group, are reproduced in Fig. 21.1. The letters D_1 through D_5 indicate the fractions of the inhaled aerosol which are either exhaled or deposited in each of the compartments. The task group finds that these fractions vary with the activity median aerodynamic diameter (AMAD) of the aerosol, and graphs are provided in the report to show this variation. The letters *a* through *j* in the diagram indicate clearance pathways from the compartments into blood, GI tract, and/or lymph. It should be noted that the pulmonary region is not a simple compartment in the usual sense of uniform mixing and elimination, since each pathway clears a prescribed fraction of the material which is deposited, and this fraction

ORNL-DWG 66-5772

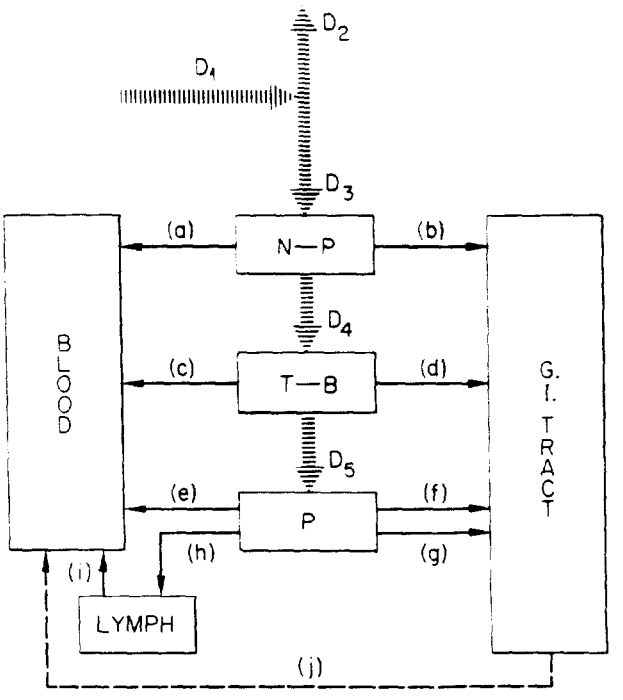

Fig. 21.1. Respiratory Tract Clearance Model.

Table 21.2. Clearance Classification

Class D, Rapid	Class W, Intermediate	Class Y, Slow
1 day to 10 days	10 days to 100 days	100 days

varies depending upon the solubility of the material deposited.

Both the amount of material following a particular route and the rate at which it is cleared are assigned on the basis of three classes of aerosols, as shown in Table 21.2. Class D material is cleared in <1 day to 10 days, class W in a matter of days or months, and class Y material over a period of months to years.

Using this model, it is a straightforward matter to calculate the microcurie-days of residence in each of the three regions for a given intake of a specified aerosol. The dose delivered to a given region in a specified time period is the product of a constant, the microcurie-days of residence during the period, and the energy absorbed per disintegration divided by the appropriate mass. These formulas for dose to the three regions during the first T days following a single intake of an aerosol follow. For the nasopharynx region:

$$D_{\text{rems}} = \frac{I \times 51 \times \epsilon}{M} \times D_3 \left(f_a \frac{1 - e^{-\lambda_a T}}{\lambda_a} + f_b \frac{1 - e^{-\lambda_b T}}{\lambda_b} \right).$$

For the tracheobronchial region:

(1) Dose from inhaled material deposited in region

$$D_{\text{rems}} = \frac{I \times 51 \times \epsilon}{M} \times D_4 \left(f_c \frac{1 - e^{-\lambda_c T}}{\lambda_c} + f_d \frac{1 - e^{-\lambda_d T}}{\lambda_d} \right);$$

(2) Dose from material cleared from P region through the T-B region to the GI tract

1147720

$$D_{\text{rems}} = \frac{I \times 51 \times \epsilon \times t}{M} \cdot D_5 \left(f_f \lambda_f^b \frac{1 - e^{-\lambda_f T}}{\lambda_f} + f_g \lambda_g^b \frac{1 - e^{-\lambda_g T}}{\lambda_g} \right).$$

For the pulmonary region:

$$D_{\text{rems}} = \frac{I \times 51 \times \epsilon}{M} \times D_5 \left(f_e \frac{1 - e^{-\lambda_e T}}{\lambda_e} + f_f \frac{1 - e^{-\lambda_f T}}{\lambda_f} + f_g \frac{1 - e^{-\lambda_g T}}{\lambda_g} + f_h \frac{1 - e^{-\lambda_h T}}{\lambda_h} \right),$$

where

I = intake at time zero (μc),

51 = dis/day × g-rad/Mev,

ϵ = effective energy per disintegration (Mev),

M = mass of region considered (g),

D_3, D_4, D_5 = fraction of the inhaled aerosol deposited in the N-P, T-B, and P regions respectively,

t = time of passage through the T-B region of material cleared from the P region to the GI tract (days),

f_a, f_b, etc. = fractions cleared by pathways a, b, etc.,

λ_a, λ_b, etc. = effective elimination constants for pathways a, b, etc.,

λ_f^b and λ_g^b = biological elimination constants for pathways f and g.

As mentioned earlier, these formulas follow directly from the definition of the new lung model except for the two factors ϵ and M, the effective energy absorbed per disintegration and the mass of the particular tissue under consideration respectively. As will be seen, it is not an entirely simple matter to decide on appropriate values for either of these parameters.

Figure 21.2 shows the accumulated dose to the pulmonary region from an instantaneous intake of 1 μc of a standard aerosol, that is, one having an AMAD of 1 μ; but in order to be perfectly general,

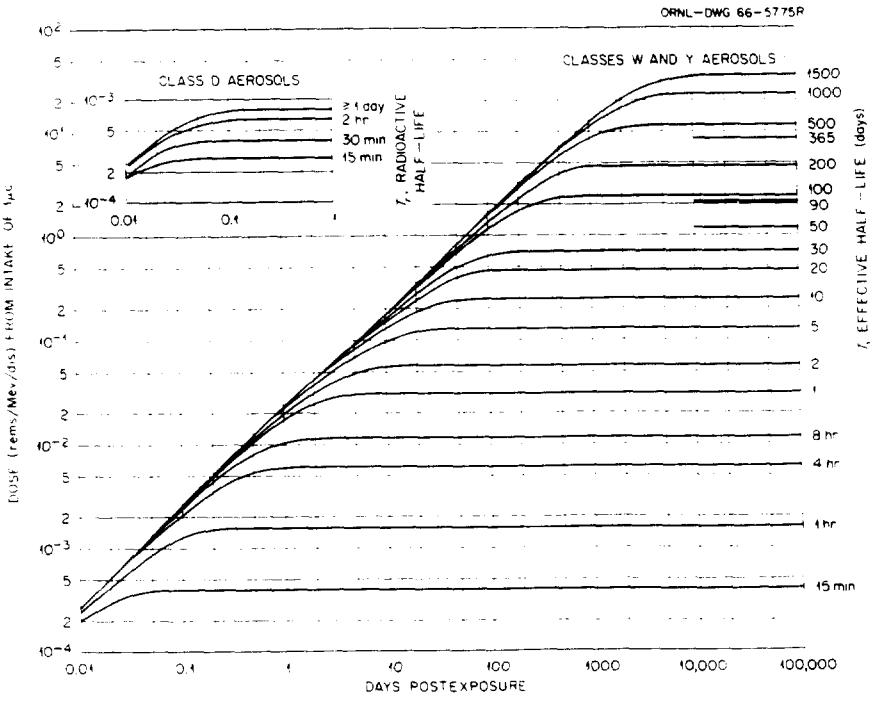

Fig. 21.2. Dose to Pulmonary Region. ϵ = 1 Mev, AMAD = 1 μ.

1147721

effective energy has been taken as 1 Mev. Thus, this graph is universally applicable for any aerosol considered in the report of the task group; one need only select the longest effective half-time for elimination from the P region, read off the ordinate for the desired time, and multiply by the appropriate effective energy. The curves for aerosols of class W or of class Y are labelled with the effective half-time, T, of the long-term component of the retention function. For example, the curve corresponding to T = 1 day really represents quite a number of different radionuclides, namely, all of those whose radioactive half-lives, together with the half-lives of the long-term pulmonary retention given in the report, are such that the effective half-time is 1 day. The terms of the formula corresponding to pathways of short elimination time might differ somewhat for some of these radionuclides, but the use of a single curve for all of them does not involve an inaccuracy of more than 5%, which is considered negligible in this context. The mass of the pulmonary region is taken as 500 g, which must be considered to include the capillary, or trapped, blood that is present there.

With a very few exceptions, the elimination half-times for an aerosol of class D do not exceed 30 min, that is, the values given in Table 4 of the report of the task group. Thus, with these very few exceptions, the dose is substantially independent of T_r except when $T_r < 1$ day. The dose to the pulmonary region from an aerosol of class D is given as an insert in Fig. 21.2, and it includes all cases except those where the report of the task group indicates a value of T_b, the biological half-time, which is substantially greater than 30 min.

The estimation of dose to the tracheobronchial region involves more novelty. The tracheobronchial tree consists of the trachea and branching bronchi down to the terminal bronchioles. It is essentially a branching tubular network. The aerosol material is carried by the mucus over the surface of these tubes as the material is cleared by ciliary action. The mass of this region is taken as 400 g, which is arrived at on the basis of estimates of volume given by Weibel[30] and others and on values for the density. Because of the intricate geometrical configuration, a significant portion of the energy released will be absorbed in neighboring tissues. This is true even in the case of an alpha emitter. For example, estimates of the surface area of the T-B region vary from 10 to 20 m^2. If one takes a layer of tissue based on this surface which is 45 μ thick, that is, the range of an alpha particle having an energy of about 5 Mev, he obtains 450 to 900 g. This is far more mass than the T-B region should have according to most estimates and indicates that a significant portion of the energy is absorbed in the surrounding tissue. The mass of 400 g is used here as an estimate of the mass of tissue lying within range of the alpha particles originating in the T-B region. The estimated dose to the T-B region from an aerosol deposited there is shown in Fig. 21.3 by the dashed curves.

In addition to this dose, material cleared from the P region to the GI tract must traverse the T-B region, and hence this material contributes dose during its passage through the region. The estimated dose to the T-B region from this source is shown in Fig. 21.3 by the smooth curves. The assumptions are as before, that is, a standard aerosol with the effective absorbed energy taken as 1 Mev. Estimates for the time of passage of the material cleared from the P region through the T-B region differ rather widely. Estimates based on observation of the movement of the material at certain sites led to estimates of a half-time for clearance of about 15 min, but this estimate may favor the more rapid elimination routes which are more readily observed. Other estimates based on gamma spectrometry indicate clearance times of

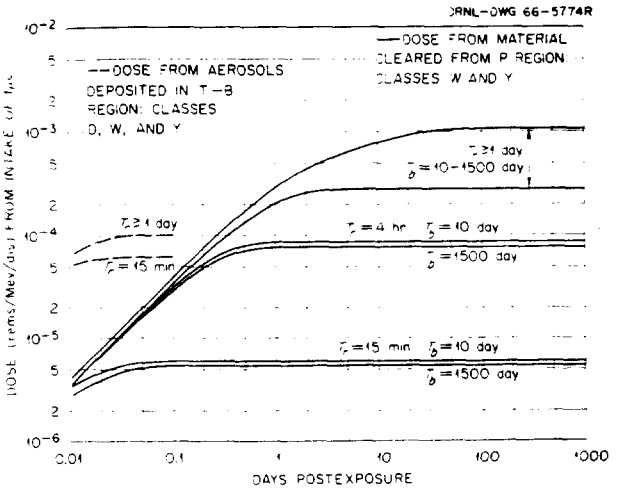

Fig. 21.3. Dose to Tracheobronchial Region. ϵ = 1 Mev, AMAD = 1 μ.

[30] E. R. Weibel, *Morphometry of the Human Lung*, Academic, New York, 1963.

1147722

2 hr or more, but these estimates may be influenced somewhat by the presence of the pulmonary deposits. Although the present dose estimate involves this uncertainty, it is clear that material passing from the P region to the GI tract makes a very significant contribution to the total dose received by the T-B region.

The N-P region consists essentially of the nasal passages and pharynx down to the level of the larynx. The aerosol merely deposits on these surfaces and is removed by the movement of the mucus. Thus a surface distribution of the material seems appropriate as a model for estimation of dose. The N-P region has about 300 cm^2 of surface, and the proposed lung model assigns a half-time of 4 min for removal of the deposited material. There is evidence that the material accumulates to a greater degree and resides longer at certain sites than at others, but in this calculation the dose is averaged over the tissue. The dose has been computed primarily for an alpha emitter, and so the dose has been averaged over a layer which is 45 μ thick. This is the range of an alpha particle having an energy of about 5 Mev. Figure 21.4 shows this dose for a standard aerosol with an effective energy of 1 Mev. Because of the short clearance time for this region, the radioactive half-life makes little difference in the dose, and essentially all of the dose is delivered within the first half hour following intake.

A certain fraction of the inhaled material is transported to the lymph nodes. For very insoluble dusts, such as those of class Y, the proposed lung model allows 10% of this material to be eliminated from the lymph nodes with a rather long half-time of 100 to 1500 days, depending on the solubility of the dust. The other 90% remains in the lymph nodes indefinitely, being subject only to radioactive decay. The dose to the lymph nodes has been computed using 15 g as the weight of these respiratory lymph nodes, a value given by Pochin[31] for the tracheobronchial lymph glands. The total mass of lymphatic material in the lung is probably larger than this, and the dose averaged over this mass somewhat smaller than that computed here. As discussed by Pochin,[31] the problem of migrating lymphocytes complicates the problem, and the facts are not in hand which might serve as the basis for a more accurate dose estimate to individual lymph nodes or lymphocytes.

[31] E. E. Pochin, *Health Phys.* 12, 563 (1966).

Figure 21.5 shows a composite of all these calculations for a very insoluble material. The curves apply to any radioactive aerosol of class Y which has the indicated AMAD and effective half-times in the P region. The effective energy per disintegration has been taken as 1 Mev. It is clear that the total dose to lymph nodes is greater than to any of the other three regions of the lungs. Even if one

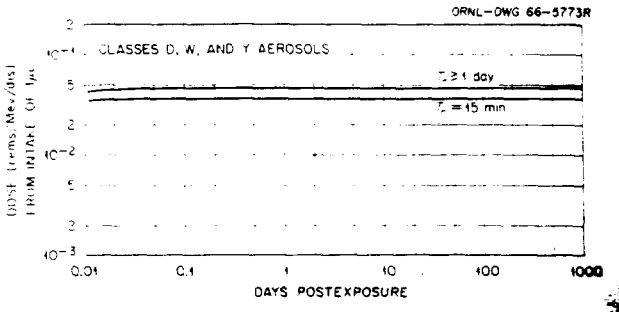

Fig. 21.4. Dose to Nasopharyngeal Region. ϵ = 1 Mev, AMAD = 1 μ.

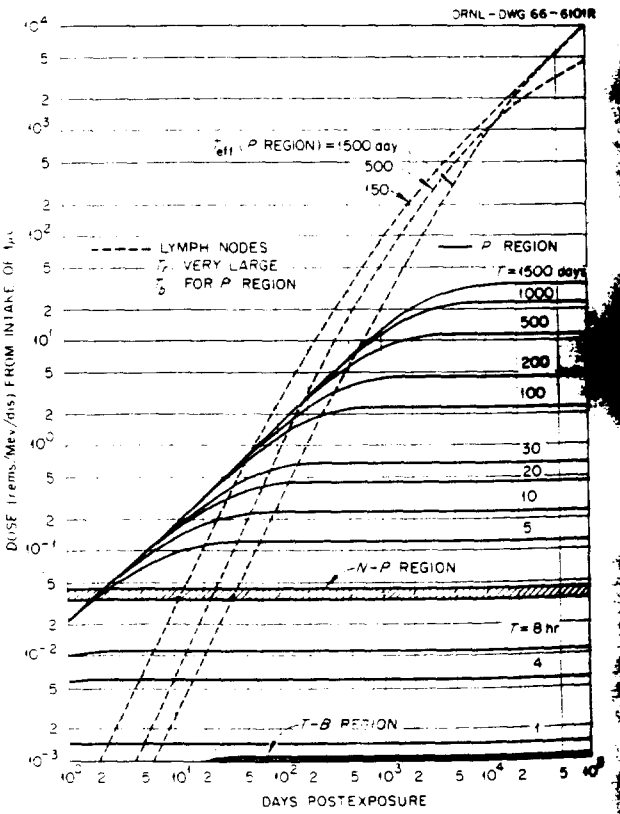

Fig. 21.5. Dose to Respiratory Tract. ϵ = 1 Mev, AMAD = 1 μ.

1147723

averages the dose over the entire lymphatic system of the body (which is not done here), the dose to the lymph predominates, but not by such a large factor.

In computing the dose curves given in Figs. 21.2–5, the AMAD has been taken as 1 μ. Since D_3 and D_5 occur as factors in the dose formula, it is possible to give a factor which corrects these curves for aerosols of other AMAD. Since $D_3 = 30$ and $D_5 = 25$ for AMAD = 1 μ, the required correction factors for the N-P and P regions are $D_3/30$ and $D_5/25$ respectively. The proposed lung model gives a constant deposition factor for the T-B region, and so factors for the pulmonary region and the N-P region are the only ones shown. It is clear that the doses vary greatly with the AMAD – the dose to the P region decreasing and that to the N-P region increasing as AMAD increases.

In the foregoing formulas and graphs the effective energy has been taken as 1 Mev. Thus each value must be multiplied by the effective energy absorbed per disintegration of the isotope in order to obtain the actual dose in rems. In the case of alpha particles it seems sufficiently accurate to take the effective energy as the total energy of the alpha particles, for the thickness of the various tissues considered will be at least of the order of the range of the particle. While individual bronchioles may have a diameter this small, these smaller ones are quite closely spaced. This is indicated clearly by considerations of surface area as noted above.

It is clear that not much of the energy of photons will be absorbed near the point of origin of the photon, and hence it seems reasonable to average the dose from photons over the entire lung. A Monte-Carlo-type code has been written to obtain the absorbed fraction of energy for photons of various energies which originate uniformly within the volume occupied by the lungs. These absorbed fractions are given in Table 21.3. A similar study has been made for a surface distribution of photons, and, as would be expected, the fraction of energy absorbed in a layer of 45-μ thickness is generally quite small.

Beta emitters clearly are somewhere between these two extremes. For a beta such as the tritium beta one may use the model for local absorption; and for a beta of long range – say, 1 cm – the model averaging over the entire lung seems more appropriate. Although it is clear that further studies of the problem are indicated, a more detailed consideration of the morphology of these regions of the lung than we have been able to find in the literature seems to be required.

Table 21.3. Absorbed Fraction for a Uniform Distribution of a Gamma Source in the Lungs of a Tissue Phantom

Energy of Gamma (Mev)	Absorbed Fraction, A. F.
0.01	0.97
0.05	0.27
0.1	0.17
0.5	0.16
1	0.15
2	0.13

VARIATION OF DOSE DELIVERED BY ^{137}Cs AS A FUNCTION OF BODY SIZE FROM INFANCY TO ADULTHOOD

H. L. Fisher, Jr. W. S. Snyder

The problem we wish to consider is the following: Given a unit source of ^{137}Cs in the body of man, determine the dose rate at various positions in his body. Since it is relatively easy to determine the beta dose rate, let us dispose of this part before we examine the gamma-dose-rate problem. In Fig. 21.6 is shown the radiological decay scheme of ^{137}Cs. The ranges of both the emitted beta particles and of the electron are less than 0.6 cm in tissue. Since this range is small compared to the dimensions of the body, we will assume, as is usually done, that the entire kinetic energy of these particles is absorbed locally. The surface skin is an exception however. Using an effective

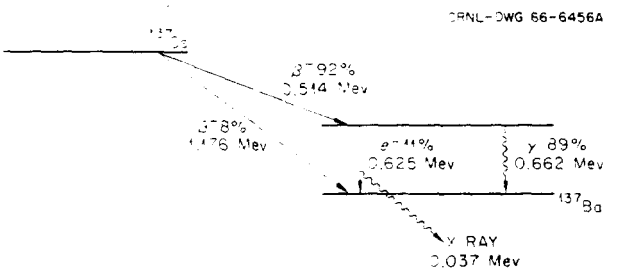

Fig. 21.6. Radiological Decay Scheme of ^{137}Cs.

1147724

energy of 0.26 Mev/dis for the betas and the electron, a dose rate of 550 microrads/hr results from a ^{137}Cs concentration in the body of 1 $\mu c/kg$. If a uniform distribution of ^{137}Cs in the body is assumed, every part of the body except the surface will be receiving a beta dose rate of 550 microrads/hr for each $\mu c/kg$ concentration of ^{137}Cs. The surface will receive about one-half of the dose rate. By way of comparison, the total-body gamma dose rate for the adult is about 480 microrads/hr per $\mu c/kg$ as we shall see later.

The problem of determining the gamma dose rate delivered to the body is not as easily resolved, because the mean range in tissue of the 0.662-Mev gamma photon is 12 cm. This value is not small compared to the dimensions of the body, so we have the problem of determining the amount of energy that escapes from the body or, conversely, the amount that is absorbed. The theory of gamma photon interaction with matter has been known for some time. However, to apply this theory to other than thin slabs and simple geometrical shapes involves elaborate mathematical calculations. Understandably, previous attempts at estimating the gamma dose rate usually have not relied on this well-developed theory but have instead employed simplifying assumptions for the purpose of performing the calculations. One such method uses the effective radius concept of the ICRP.[27] The body or organ is assumed to be a sphere of tissue of a given radius with the entire organ burden located at its center. A first-collision calculation of dose to this sphere of tissue is then effected. This method conservatively estimates the gamma dose to the body from ^{137}Cs to be about twice as high as has been found in this report.

Through the use of the high-speed digital computer it has become practical to apply the well-developed theory of gamma photon interaction with matter and dispense with many simplifying assumptions. However, we still need to specify the shape of the human body. In Fig. 21.7 is shown the type of phantom and coordinate system we have chosen. The head and neck are represented by the upper elliptical cylinder; the trunk and arms compose the elliptical cylinder of the center section; and the legs below the buttocks form the elliptical cone of the phantom. This form of the phantom is the same for all ages. Only the heights and axes of the elliptical cylinders and elliptical cone are varied to provide a phantom approximating the body size of grossly normal individuals ranging in age from infancy to adulthood. For this problem, six phantoms representing body sizes of human males of ages 0, 1, 5, 10, 15, and 20 years were constructed. The weights and dimensions completely specifying the phantoms are given in Fig. 21.7. These dimensions were chosen after considering data on body weight, length, breadth, and circumference of body parts obtained from the *Biological Handbook* by Altman.[32] Reference material also was obtained from the phantom constructed by Hayes and Brucer.[33] Data on the relative volume of body parts were obtained from "Growth of Man" in *Tabulae Biologicae* by Krogman.[34]

As shown in Fig. 21.7 the phantom was divided into over a hundred subregions in which the dose rate was determined. There are four layers in the legs in which the dose rate was calculated. There were usually five layers in the trunk section. However, in phantoms for ages 0, 1, and 5 years the trunk was divided into three, three, and four layers, respectively, in order to obtain a reasonably accurate estimate of dose rate in each. Inside the trunk the layers are further subdivided into five concentric bands. These bands are further cut by vertical cross planes to give the final and smallest volume elements in which dose rate was determined. The head section was sectioned into either two or four layers, depending on head size. With this subdivision of the phantom, the vertical variation of dose rate could be determined as well as the the side-to-side and front-to-back variations.

A Monte-Carlo-type method of calculating the dose rate was used. This code is similar to the one used by Ellett, Callahan, and Brownell,[35] the phantom used here is different. The gamma attenuation coefficients for the medium were taken from Grodstein.[36] This method requires that the flight of a photon is mathematically followed between interaction sites. Through probabilistic

[32] P. L. Altman and D. S. Dittmer, *Growth Including Reproduction and Morphological Development*, Biological Handbook, Fed. Am. Soc. Exptl. Biol., Washington, 1962.

[33] R. L. Hayes and M. Brucer, *Intern. J. Appl. Rad. Isotopes* 9, 111 (1960).

[34] W. M. Krogman, "Growth of Man," pp. 712–15 in *Tabulae Biologicae*, vol. XX, ed. by H. Denzer *et al.*, Den Haag, 1941.

[35] W. H. Ellett, A. B. Callahan, and G. L. Brownell, *Brit. J. Radiol.* 37(433), 45 (1964).

[36] G. W. Grodstein, *X-Ray Attenuation Coefficients for 10 kev to 100 Mev*, NBS Circular 583, 1957; and R. T. McGinnis, *Supplement to NBS Circular 583*, 1959.

1147725

times. Suppose a photon, $P_{n-1} = P(x_{n-1}, y_{n-1}, z_{n-1}, a_{n-1}, b_{n-1}, L_{n-1}, E_{n-1}, W_{n-1})$, is in flight between points $n-1$ and n. We wish to know the energy deposition at point n and the location of the point $n+1$, which may be found if we find P_n and use it in conjunction with P_{n-1}. The coordinates x_n, y_n, and z_n may be found by applying algebraic geometry using x_{n-1}, y_{n-1}, z_{n-1}, a_{n-1}, b_{n-1}, and L_{n-1}. The new direction of flight, a_n and b_n, is determined by using E_{n-1} and the Klein-Nishina gamma photon scattering distribution. The new energy E_n is calculated from the angle of scatter, which involves a_{n-1}, b_{n-1}, a_n, and b_n. Length L_n is calculated as follows:

$$L_n = \frac{-1}{\sigma(E_n)} \ln N ,$$

where $\sigma(E_n)$ is the attenuation cross section of the medium and N is a random number chosen uniformly on $0 \leq N \leq 1$. The weight W_n is given by

$$W_n = W_{n-1} \frac{\sigma_c(E_n)}{\sigma(E_n)} ,$$

where $\sigma_c(E_n)$ is the cross section for the Compton process. The energy deposition at point n is

$$E\Delta = W_{n-1} \left[\frac{\sigma_p(E_{n-1})}{\sigma(E_{n-1})} E_{n-1} - \frac{\sigma_c(E_{n-1})}{\sigma(E_{n-1})} (E_{n-1} - E_n) + \frac{\sigma_{pp}(E_{n-1})}{\sigma(E_{n-1})} (E_{n-1} - 2e) \right] ,$$

where $\sigma_p(E_n)$, $\sigma_c(E_n)$, and $\sigma_{pp}(E_n)$ are the cross sections for the photoelectric, Compton, and pair production processes, respectively, and e is the rest mass of an electron in energy units. The total flight history of a photon may end in one of three ways. It may end by escaping from the phantom, or when its energy falls below 2 kev, or when its weight falls below 10^{-5}.

Let us look briefly at the restrictions of this method as we are using it. Other than the obvious inaccuracies that the shape of the phantoms only roughly approximates the shape of the human body and that the phantom remains in a fixed standing position and is in free space from which no backscatter occurs, there is one restriction that should be emphasized. This phantom is homogeneous throughout. There is no low density and low cross-sectional area for the lungs, nor is there a high density and modified cross-sectional area for bone. To take these into account would involve a rewriting of the entire code. Although the results obtained with the constant-density phantom will need to be refined in the future, the results presented here are an improvement over past ones.

In Fig. 21.8 is a graph of the total-body gamma dose rate vs age from a ^{137}Cs source uniformly distributed in the phantoms. The units of the ordinate are in dose rate (microrads/hr) per unit activity concentration in the body (μc/kg). Dose rates for the different phantoms are given per unit concentration of activity in the phantoms, but one may convert the values given to other bases of comparison. Throughout this paper we will use the units just described. It is the primary purpose of this report to describe the physical differences in gamma-ray absorption in different size phantoms although biological parameters such as biological half-life, gut absorption, and intake quantity will influence a hazards evaluation.

From this graph we see that the total-body dose rate for the infant is slightly less than one-half that for the adult. This is due to the fact that the 0.662-Mev gamma rays have a higher probability

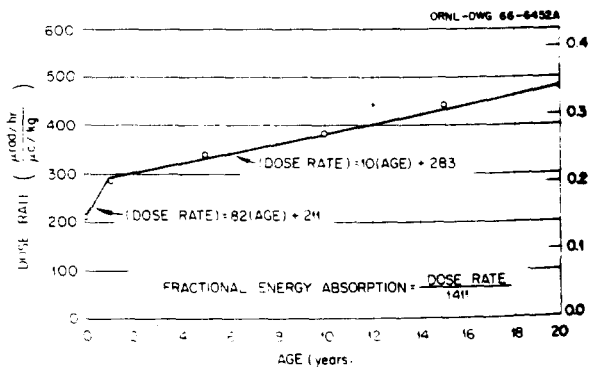

Fig. 21.8. Average Total-Body Gamma Dose Rate from a Uniformly Distributed ^{137}Cs Source.

1147727

ORNL-DWG 66-6436

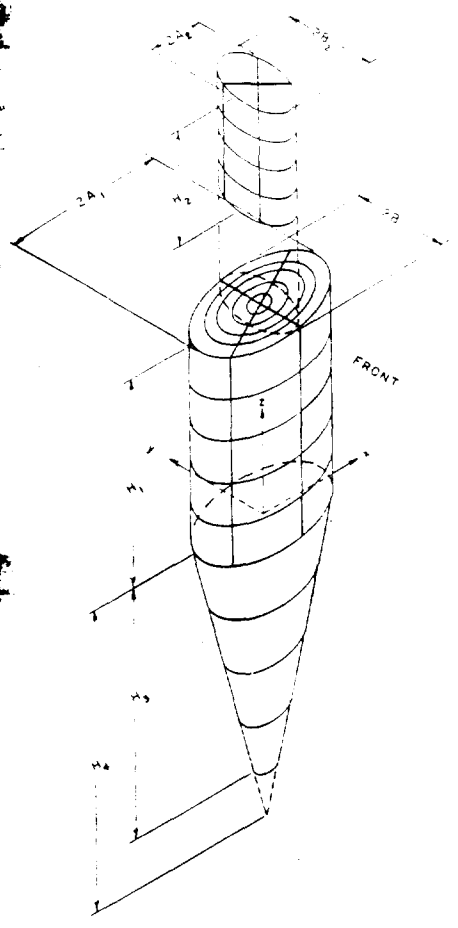

PHANTOM DIMENSIONS AND DOSE REGIONS

Age (yr)	Weight (kg)	H_1 (cm)	H_2 (cm)	H_3 (cm)	H_4 (cm)	A_1 (cm)	B_1 (cm)	A_2 (cm)	B_2 (cm)
0	3.473	23	13	15	20	5.5	5	4.5	5
1	10.171	33	16	27	36	8	7	6.5	7
5	19.654	45	20	46	57.5	11	7.5	6.5	7.5
10	31.902	54	22	64	80	14	8	6.5	8
15	54.041	65	23	78	97.5	18	9	7	9
20	70.037	70	24	80	100	20	10	7	10

Fig. 21.7. Phantom Dimensions and Dose Regions.

rules, the energy deposition of the photon at an interaction site is recorded. After a large number of such simulated photon histories have been calculated, the average energy deposition per photon in a region is then estimated, and the dose per photon may be calculated. Photons of initial energy 0.662 Mev were randomly generated uniformly in the phantoms as follows: 80,000 in the phantoms for ages of 15 and 20 years; 100,000 in the phantoms for ages 1, 5, and 10 years; and 160,000 in the phantom for the newborn. For each photon the direction of flight was selected randomly. The flight distance to the first interaction site was determined randomly using the cross section of the medium at the energy of the photon. After selecting a new flight direction emanating from this interaction site probabilistically from the Klein-Nishina distribution, the energy deposition at this site can be determined. The process of photon flight is now repeated but with a decreased energy. Let $n - 1$, n, and $n + 1$ be consecutive interaction sites for a photon. The mathematical photon is characterized by eight independent quantities – x, y, and z, the coordinates of the present interaction site; a and b, the direction cosines specifying the direction of flight to the next interaction site; L, the length of the photon's flight path to the next interaction site; E, the energy of the photon during its flight; and W, the weight of the photon during its flight. The weight of a mathematical photon is the probability the photon exists and takes on all values from zero to 1. It is set equal to 1 for a photon just started from the source. However, a real photon has a weight of either zero or 1 at all

1147726

escaping from the infant phantom than from the adult phantom, which is 20 times larger in the total mass. The total-body dose rate for the adult as determined by this Monte Carlo calculation is about one-half that obtained by an ICRP effective radius calculation. At this point let us refer to the gamma plus beta dose rate. The total dose rate from ^{137}Cs may be obtained by adding 550 to the values given on this graph or on any succeeding dose rate graph for a uniformly distributed source presented in this report. This is true for all of the phantoms.

Since a Monte Carlo computation is an involved and time-consuming procedure, it is more efficient to store the results of the calculation for application to other problems. The results have been stored in three modes – graphically, in tables, and in approximating formulas. As seen in the graph, the gamma dose rate vs age has been approximated by two linear functions. There is no theoretical significance to these approximating functions. They are used as a convenient means of storing the data simply and for retrieving them within a certain range of error.

To show the variation of dose within the phantoms, we have chosen the results for the infant and adult phantoms only. Results for the other phantoms are similar to these two. We shall examine results from the adult phantom first. In Fig. 21.9 is a graph of the average dose rate in horizontal layers from head to foot of the phantom. The error bars on the Monte Carlo points are one standard deviation due to the statistical variability involved in Monte Carlo calculations. We note particularly that the average dose rate along the trunk is nearly constant and is about 15% greater than the average dose rate for the total body. The top of the head and bottom of the feet receive the lowest dose rate, being about a factor of 3 below the trunk average. The Monte Carlo points above those for the layer average are the dose rates along the vertical axis of the trunk. At this location, in the interior, are found the highest dose rates in the body. These are higher than the layer average by about 30%. Let us examine the approximate gonadal gamma dose rates. The ovaries, which would be located near the vertical axis of the trunk, receive this central dose rate. The testes receive a dose rate that is approximately that of the trunk average. As a point of perspective, the vertical distribution of gamma dose rate in the infant has been plotted on this same graph.

The variation of dose rate from the center of the trunk to its surface for the adult phantom is given in Fig. 21.10. Because little variation in dose rate exists among the layers of the trunk, we may average the values from all layers to obtain better statistics. This was done, and the two curves seen here are the dose rates from the center to the front surface and from the center to the side surface. Of course, the dose rate from center to back is identical with the center-to-front dose rate and has been included. Similar remarks apply to the

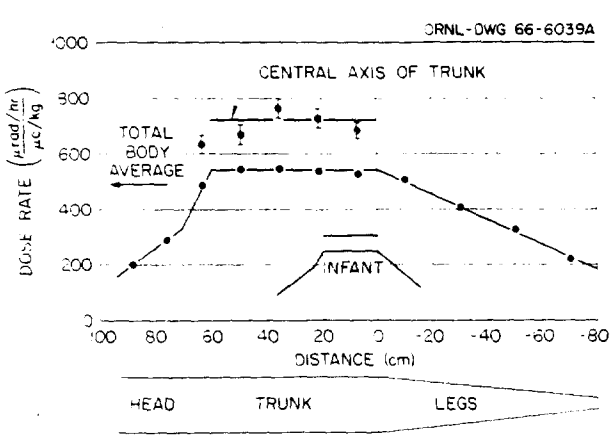

Fig. 21.9. Average Gamma Dose Rate in Horizontal Layers in the Adult Phantom from a Uniformly Distributed ^{137}Cs Source.

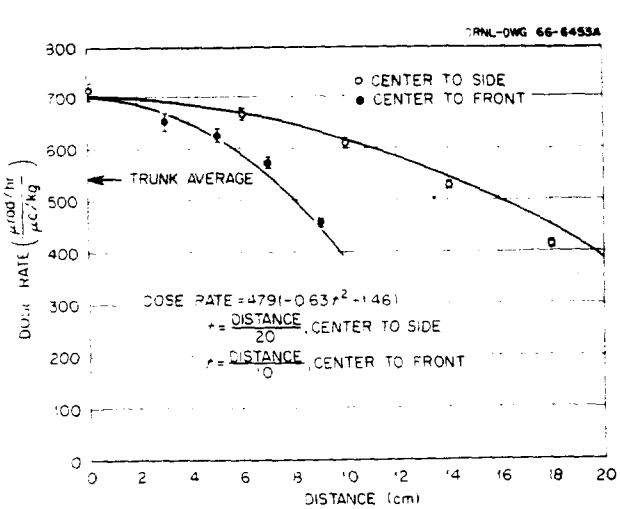

Fig. 21.10. Gamma Dose Rate from Center to Surface of Adult Phantom from a Uniform ^{137}Cs Source.

1147728

variation of dose from left to right. From the Monte Carlo estimates, it was noted that the dose rate at the front surface was not very different from that at the side surface. Considering that the trunk is elliptical and twice as wide as it is thick, this result was a little surprising. The other phantoms are not as highly elliptical, and this result is valid for them also. The dose rate at the surface is about one-half the central dose rate.

In Fig. 21.11 is shown the vertical variation of dose rate in the infant phantom. It appears that the relative changes observed from head to foot are about the same as for the adult phantom. However, the entire graph is located at a lower dose rate than the one for the adult. The variation of dose rate from center to surface of the infant phantom is given in Fig. 21.12. Since the infant trunk is nearly cylindrical, being only 1 cm wider than it is thick, there is practically no difference in the center-to-front and center-to-side data. Again, the surface dose rate is about one-half the central dose rate.

Results from the other four phantoms are similar to the ones already shown. Results from all phantoms are shown in Fig. 21.13; also shown here is the normalized dose rate for each phantom. Zero on the abscissa is the center axis of the trunk, while the value 1 is the surface. To normalize the dose rate for a phantom, we divide by the total-body dose rate for that phantom. It may be observed that the variation of dose rates among the phantoms is about 10% after normalization in the manner described.

The equations approximating the data you have seen in the preceding graphs are tools that allow one to retrieve with sufficient accuracy the results found by the Monte Carlo method. All of these equations are given compactly in Fig. 21.14. The first function relates age to total-body gamma dose rate; the second function permits calculation of the average gamma dose rate from foot to head of the phantom; and the third function gives the gamma dose rate at any position inside the trunk. Functions 4 and 5 are derivable from 3, while function 6 is the beta dose rate.

Let us now consider a nonuniform distribution of ^{137}Cs in the phantom. It has been found by Yamagata[37] that the cesium concentration of muscle is

[37] N. Yamagata, *Radiation Res.* 3–1, 9 (March 1962).

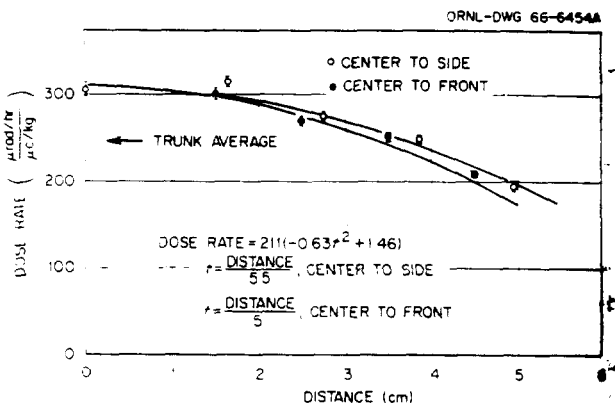

Fig. 21.12. Gamma Dose Rate from Center to Surface of Infant Phantom from a Uniform ^{137}Cs Source.

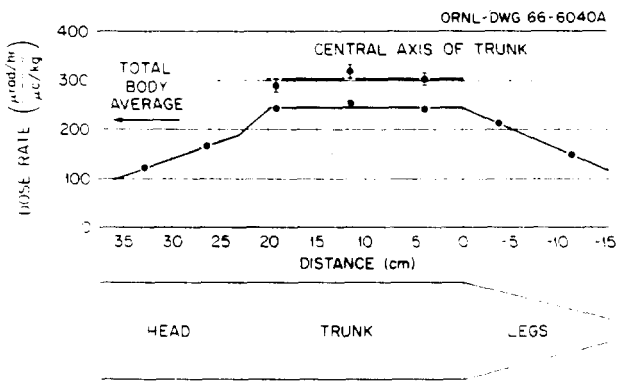

Fig. 21.11. Average Gamma Dose Rate in Horizontal Layers in the Infant Phantom from a Uniformly Distributed ^{137}Cs Source.

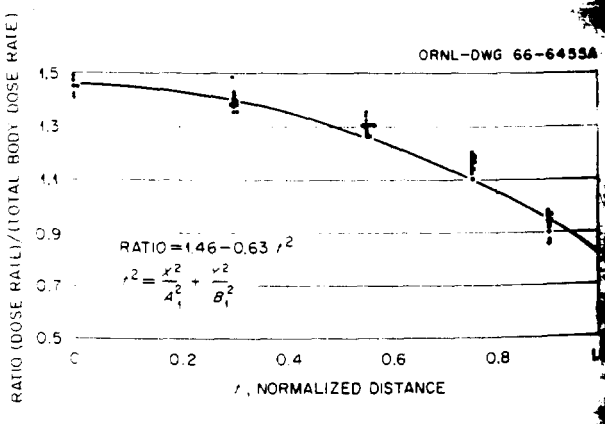

Fig. 21.13. Normalized Gamma Dose Rate from Center to Surface of Normalized Phantoms from a Uniform ^{137}Cs Source.

1147729

1141130

$$(1)\quad D_{avtb} = \begin{cases} 82\,(\text{Age, yr}) + 211 \pm 5\%, & 0 \le \text{Age} \le 1 \\ 10\,(\text{Age, yr}) + 283 \pm 5\%, & 1 \le \text{Age} \le 20 \\ 483, & 20 \le \text{Age} \end{cases}$$

$$(2)\quad D_{av}(Z) = \begin{cases} D_{avtb}\left[\dfrac{0.72}{H_3} Z + 1.15\right] \pm 25\%, & -H_3 \le Z \le 0 \\ D_{avtb}\left[1.15\right] \pm 5\%, & 0 \le Z \le \dfrac{6}{7} H_1 \\ D_{avtb}\left[-\dfrac{2.47}{H_1} Z + 3.25\right] \pm 20\%, & \dfrac{6}{7} H_1 \le Z \le H_1 \\ D_{avtb}\left[-Z + H_1 + 2H_2\right] \dfrac{0.40}{H_2} \pm 20\%, & H_1 \le Z \le H_2 \end{cases}$$

$$(3)\quad D(x,y) = D_{avtb}\left[-0.63\left(\frac{x^2}{A_1^2} + \frac{y^2}{B_1^2}\right) + 1.46\right] \pm 10\%, \qquad 0 \le Z \le \frac{6}{7} H_1, \quad \frac{x^2}{A_1^2} + \frac{y^2}{B_1^2} \le 1$$

$$(4)\quad D_{center} = 1.46\, D_{avtb} \pm 10\%$$

$$(5)\quad D_{surface} = 0.83\, D_{avtb} \pm 10\%$$

$$(6)\quad D_{\beta} = 550$$

where

D_{avtb} is the total body gamma dose rate

$D_{av}(Z)$ is the gamma dose rate in horizontal layers along the vertical axis Z

$D(x,y)$ is the gamma dose rate at the position (x,y) in the trunk

D_{center} is the gamma dose rate along the Z axis in the trunk

$D_{surface}$ is the gamma dose rate at the surface of the trunk

D_{β} is the beta dose rate everywhere in the phantom

Fig. 21.14. Dose Rate (μrad/hr per μc/kg) in Phantoms from a ^{137}Cs Source Uniformly Distributed in the Phantoms.

about twice that of other soft tissues, the latter being fairly uniform. To simulate this distribution in the adult phantom, the volume of the leg section and about one-half of the trunk volume nearest the surface were taken to represent muscle. The equation separating these volumes is

$$\left(\frac{X}{14}\right)^2 + \left(\frac{Y - 1.5}{7}\right)^2 = 1.$$

In this muscle section the source concentration of ^{137}Cs was twice the remaining sections. Surprisingly, this distribution of the source did not produce any large change in the gamma dose rate anywhere in the body when compared with the uniform distribution of the same body burden. For example, the total-body dose rate for the nonuniform distribution was 2% less than that for the uniform case, while the dose rate along the central axis of the trunk for the nonuniform case was 90% of that in the uniform case. However, the beta dose rate would be twice as large in the muscle as in other soft tissue since all beta energy was assumed to be absorbed locally.

Let us close by considering the total-body beta plus gamma dose received by the infant and the adult when each takes in 1 μc of ^{137}Cs. Let us assume the gut absorption to be 100% and the biological half-times of cesium to be 100 days for the adult and 20 days for the infant. In this case the infant would receive 0.15 rad and the adult 0.05 rad; that is, the infant would receive three times the dose received by the adult.

We see that although the infant receives the same beta dose rate and only one-half the gamma dose rate as the adult per unit ^{137}Cs body concentration, metabolic parameters as well as intake patterns need to be included in the analysis to arrive at meaningful conclusions as to dose commitment or assessment of risk.

Acknowledgement

Appreciation for the coding and computer operations is expressed to Gordon G. Warner of the ORNL Mathematics Division.

IODINE RETENTION

W. S. Snyder H. L. Fisher, Jr.
Monica Boyd

Therapeutic and diagnostic use of radioactive iodine, as well as that available to the population through fallout and the food chain, provides impetus for the study of iodine retention by the thyroid and the body. Several models have been proposed[38,39] which consist of essentially three compartments. It is the purpose of this report to give solutions for the iodine retention model in general and in detail, using typical or normal metabolic parameters.

The model is shown schematically in Fig. 21.15. The Q's are the quantities of iodine in the various compartments, and the K's are rate constants by which transfer occurs between compartments. The system of differential equations governing the kinetics is:

$$\frac{d}{dt} Q_I(t) = -(K_{IE} + K_{IG} + \lambda)\, Q_I(t) + K_{BI}\, Q_B(t)\,,$$

$$\frac{d}{dt} Q_G(t) = K_{IG}\, Q_I(t) - (K_{GB} + \lambda)\, Q_G(t)\,, \qquad (1)$$

$$\frac{d}{dt} Q_B(t) = K_{GB}\, Q_G(t) - (K_{BI} + K_{BF} + \lambda)\, Q_B(t)\,.$$

This system is valid for radioactive iodine with decay constant λ or for stable iodine with $\lambda =$

[38] G. L. Brownell, *J. Clin. Endocrinol. Metab.* 11, 10[illegible] (1951).

[39] D. S. Riggs, *Pharmacol. Rev.* 4, 284 (1952).

ORNL-DWG 66-[illegible]

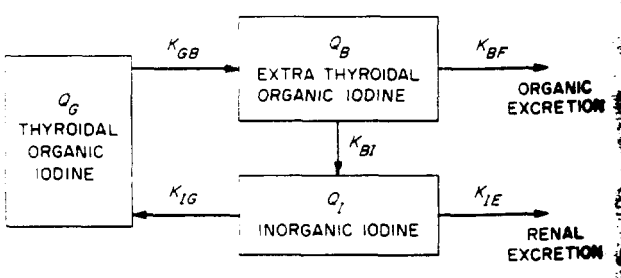

Fig. 21.15. Compartmental Model for Iodine Metabolism.

1147731

activity in a compartment may be obtained by multiplying the quantities Q by λ. This system will be solved for the case of an intake of inorganic iodine of amount $Q_I(0)$ into the inorganic iodine compartment at time zero. The initial conditions are therefore:

$$Q_I(0) = Q_I(0) ,$$

$$Q_G(0) = 0 ,$$

$$Q_B(0) = 0 .$$

It is appropriate to emphasize again that this model is for the normal thyroid under normal conditions and may not apply to pathological cases or people on high- or low-iodine diets. The solution to the system is:

$$Q_I(t) = Q_I(0)\frac{1}{D}\left\{(K_{GB} - \lambda_1)Ae^{-(\lambda_1 + \lambda)t} + (K_{GB} - \lambda_2)Be^{-(\lambda_2 + \lambda)t} + (K_{GB} - \lambda_3)Ce^{-(\lambda_3 + \lambda)t}\right\} ,$$

$$Q_G(t) = Q_I(0)\frac{1}{D}\left\{K_{IG}Ae^{-(\lambda_1 + \lambda)t} + K_{IG}Be^{-(\lambda_2 + \lambda)t} + K_{IG}Ce^{-(\lambda_3 + \lambda)t}\right\} ,$$

$$Q_B(t) = Q_I(0)\frac{1}{D} \times \left\{(K_{GB} - \lambda_1)(K_{IG} + K_{IE} - \lambda_1)Ae^{-(\lambda_1 + \lambda)t} + (K_{GB} - \lambda_2)(K_{IG} + K_{IE} - \lambda_2)Be^{-(\lambda_2 + \lambda)t} + (K_{GB} - \lambda_3)(K_{IG} + K_{IE} - \lambda_3)Ce^{-(\lambda_3 + \lambda)t}\right\} ,$$

where

$$D = (\lambda_1 - \lambda_2)[\lambda_3(\lambda_1 + \lambda_2 - \lambda_3) - \lambda_1\lambda_2] ,$$

$$A = (\lambda_2 - \lambda_3)[K_{GB} + K_{IG} + K_{IE} - (\lambda_2 + \lambda_3)] ,$$

$$B = (\lambda_3 - \lambda_1)[K_{GB} + K_{IG} + K_{IE} - (\lambda_3 + \lambda_1)] ,$$

$$C = (\lambda_1 - \lambda_2)[K_{GB} + K_{IG} + K_{IE} - (\lambda_1 + \lambda_2)] ,$$

and λ_1, λ_2, and λ_3 are the three solutions of

$$-\lambda^3 + (K_{GB} + K_{IE} + K_{IG} + K_{BI} + K_{BF})\lambda^2 - (K_{GB}K_{BI} + K_{GB}K_{BF} + K_{GB}K_{IE} + K_{GB}K_{IG} + K_{IE}K_{BI} + K_{IE}K_{BF} + K_{IG}K_{BI} + K_{IG}K_{BF})\lambda - (K_{IE}K_{GB}K_{BI} + K_{IE}K_{GB}K_{BF} + K_{IG}K_{GB}K_{BF}) = 0 .$$

Riggs[39] has given typical values determined from experiment for the transfer rates for the normal thyroid and for several pathological conditions. These rates for the normal individual given in units of proportion per hour are:

$$K_{IG} = 0.0389 ,$$
$$K_{IE} = 0.0800 ,$$
$$K_{GB} = 0.000364 ,$$
$$K_{BI} = 0.00222 ,$$
$$K_{BF} = 0.000208 .$$

Using these constants the retention in the three compartments of any isotope of iodine with radiological decay constant λ (hr^{-1}) is:

$$Q_I(t) = Q_I(0)\{1.00e^{-(0.119 + \lambda)t} - 0.00093e^{-(0.00255 + \lambda)t} + 0.00093e^{-(0.000246 + \lambda)t}\} ,$$

$$Q_G(t) = Q_I(0)\{-0.328e^{-(0.119 + \lambda)t} + 0.016e^{-(0.00255 + \lambda)t} + 0.312e^{-(0.000246 + \lambda)t}\} ,$$

1147732

$$Q_B(t) = Q_I(0)\,\{-0.0027e^{-(0.119+\lambda)t} - 0.0478e^{-(0.00255+\lambda)t} + 0.0505e^{-(0.000246+\lambda)t}\},$$

where t is in hours.

For ^{131}I, $\lambda = 0.00359\ hr^{-1}$ and $A(t) = \lambda\, Q(t)$ where $A(t)$ is the activity, the retention equations are:

$$A_I(t) = A_I(0)\,\{1.00e^{-0.122t} - 0.00093e^{-0.00614t} + 0.00093e^{-0.00384t}\},$$

$$A_G(t) = A_I(0)\,\{-0.328e^{-0.122t} + 0.016e^{-0.00614t} + 0.312e^{-0.00384t}\},$$

$$A_B(t) = A_I(0)\,\{-0.0027e^{-0.122t} - 0.0478e^{-0.00614t} + 0.0505e^{-0.0384t}\},$$

where t is in hours.

These retention functions are shown graphically in Figs. 21.16 to 21.18. The equilibrium level in a compartment model may be computed if the intake rate, I, is known. Let

$$\frac{d}{dt}Q(t) = -\Lambda\, Q(t) \qquad (2)$$

be the matrix formulation of the system of differential equations representing the model. Then for constant intake rate, M,

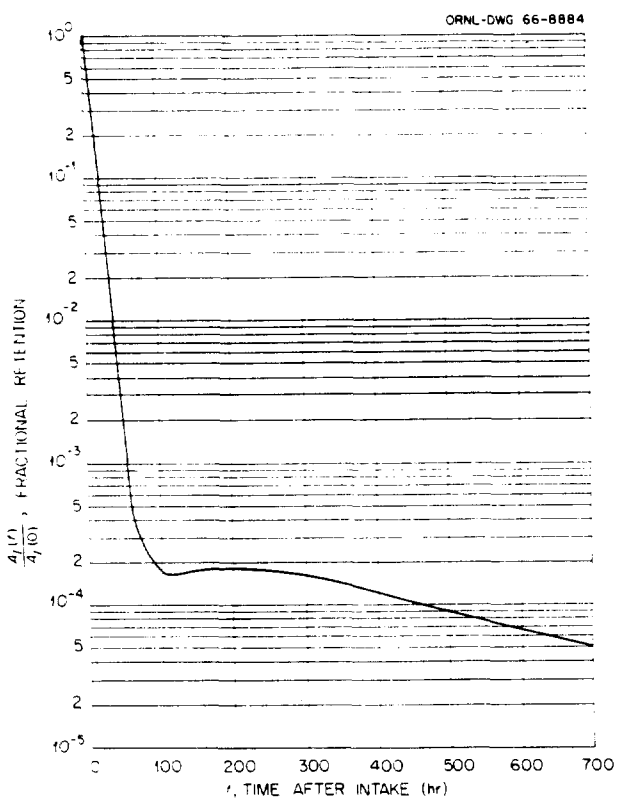

Fig. 21.16. Fractional Retention of Inorganic ^{131}I After Single Intake.

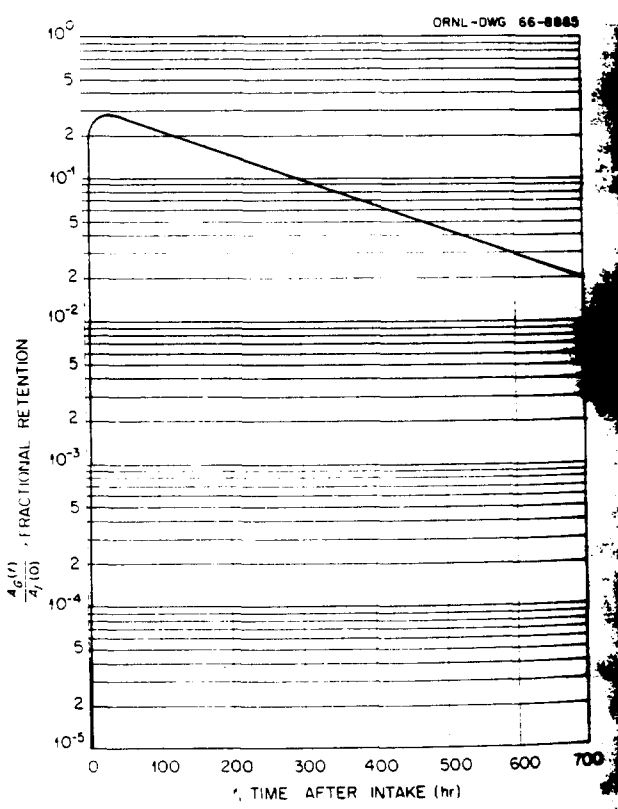

Fig. 21.17. Fractional Retention of Thyroidal Organic ^{131}I After Single Intake.

1147733

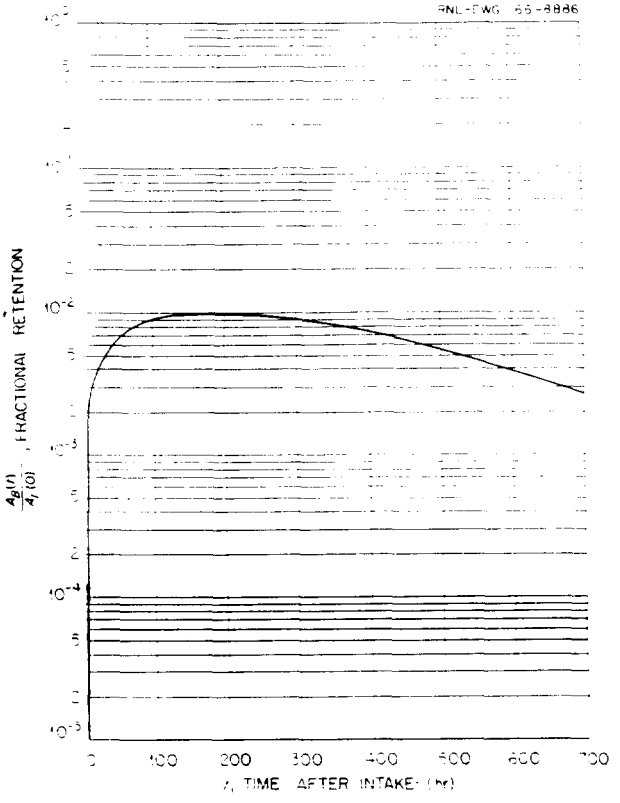

Fig. 21.18. Fractional Retention of Extrathyroidal Organic ^{131}I After Single Intake.

$$\frac{d}{dt}Q(t) = -\Lambda\, Q(t) + M\,,$$

$$\left.\frac{d}{dt}Q(t)\right]_{t=\infty} = -\Lambda\, Q(\infty) + M\,. \tag{3}$$

It has been shown by Berman and Schoenfeld[40] that for a Λ whose elements satisfy

$$\lambda_{ij} \leqq 0,\ i \neq j\,,$$

$$\lambda_{ii} \leqq \sum_{\substack{j=1\\ j\neq i}}^{n} \lambda_{ji}\,,$$

the roots, x, of $|\Lambda - xI| = 0$ have negative real parts and that pure imaginary roots are impossible. Consequently the solutions of (2) consist of sums of exponentials with negative powers, while (3) is of the same form plus a constant. Therefore,

$$\left.\frac{d}{dt}Q(t)\right]_{t=\infty} = 0\,.$$

and the equilibrium activity is

$$Q(\infty) = \Lambda^{-1}M\,.$$

In the case of the three-compartment system for iodine, the equilibrium activity, $A(\infty) = \lambda\, Q(\infty)$, for a constant continuous intake is:

$$\begin{bmatrix} A_I(\infty) \\ A_B(\infty) \\ A_G(\infty) \end{bmatrix} = \frac{I_I}{S}\begin{bmatrix} (K_{BI} + K_{BF} + \lambda)(K_{GB} + \lambda) \\ K_{GB}K_{IG} \\ (K_{BI} + K_{BF} + \lambda)K_{IG} \end{bmatrix},$$

where

$$S = (K_{BI} + K_{BF} + \lambda)(K_{IG} + K_{IE} + \lambda)(K_{GB} + \lambda) - K_{BI}K_{GB}K_{IG}\,,$$

I_I = activity/hr intake into inorganic iodine compartment.

For ^{131}I

$$\begin{bmatrix} A_I(\infty) \\ A_B(\infty) \\ A_G(\infty) \end{bmatrix} = I_I \begin{bmatrix} 11.6 \\ 6.9 \\ 114 \end{bmatrix}.$$

The percentage of the ^{131}I body burden in each compartment at equilibrium is, therefore, 8.7% inorganic, 5.2% extrathyroidal organic, and 86.1% thyroidal organic. For stable iodine, $\lambda = 0$, the equilibrium amounts (g) for a constant continuous intake, M_I (g/hr), are:

$$\begin{bmatrix} Q_I(\infty) \\ Q_B(\infty) \\ Q_G(\infty) \end{bmatrix} = M_I \begin{bmatrix} 12 \\ 192 \\ 1280 \end{bmatrix}.$$

The percentage of the stable iodine body burden in each compartment at equilibrium, therefore, is 0.8%

[40] M. Berman and R. Schoenfeld, *J. Appl. Phys.* 27(11), 1361 (1956).

1147734

inorganic, 13% extrathyroidal organic, and 86.2% thyroidal organic.

The total dose to any compartment of a compartmental model from a single intake may be calculated. Let the system

$$\frac{d}{dt} A(t) = -\Lambda\, A(t)$$

with initial conditions $A(0)$ describe this model, where $A(t)$, column vector, is the activity (μc) and Λ the decay matrix (hr^{-1}). Then

$$\int_0^\infty \frac{d}{dt} A(t)\, dt = -\Lambda \int_0^\infty A(t)\, dt\,,$$

$$[A(\infty) - A(0)] = -\Lambda \int_0^\infty A(t)\, dt\,.$$

For the reasons mentioned previously, the solution $A(t)$ consists of exponentials with exponents consisting of negative real parts. Therefore, the μc-hr of residence is

$$\int_0^\infty A(t)\, dt = \Lambda^{-1} A(0)\,,$$

and the total dose in rads D_i to compartment i from a single intake may be obtained from

$$\begin{bmatrix} D_1 m_1 \\ D_2 m_2 \\ \vdots \\ D_n m_n \end{bmatrix} = 2.13\epsilon\, \Lambda^{-1} A(0)\,,$$

where ϵ is the effective energy in Mev and m_i the compartment mass. For the three-compartment model for iodine, the total dose (rads) to each compartment from a single intake is:

$$\begin{bmatrix} D_I \\ D_B \\ D_G \end{bmatrix} = \frac{2.13\, A_I(0)}{S} \begin{bmatrix} (K_{BI} + K_{BF} + \lambda)(K_{GB} + \lambda)/M_I \\ K_{GB} K_{IG}/M_B \\ (K_{BI} + K_{BF} + \lambda) K_{IG}/M_G \end{bmatrix},$$

where M_I, M_B, and M_G are the masses of the three compartments I, B, and G; $A_I(0)$ is the initial amount of activity (μc) introduced into compartment I; and

$$S = (K_{BI} + K_{BF} + \lambda)(K_{IG} + K_{IE} + \lambda)(K_{GB} + \lambda) - K_{BI} K_{GB} K_{IG}\,.$$

Assuming the thyroid to weigh 20 g, the total dose from organic thyroidal iodine from a single intake of ^{131}I is:

$$\frac{D_G}{A_I(0)} = 2 \text{ rads}/\mu c\,.$$

Conclusion

The mathematical equations for a three-compartmental model for iodine metabolism were solved to find the retention functions for the compartments using typical parameters for thyroid function. The equilibrium level for each compartment under constant continuous intake conditions was found as a rational function of the compartmental transfer constants. The activity residence time or total dose for each compartment from a single intake was also found as a rational function of the compartmental transfer coefficients. These equations were given as a function of the radiological decay constant, permitting their use with any radio- or stable isotope of iodine. The use of these equations was demonstrated by employing ^{131}I as an example.

COMPUTER STUDIES OF LINEAR COMBINATION OF EXPONENTIALS REPRESENTING POWER FUNCTIONS

S. R. Bernard W. Davis III

This study was undertaken to compare a sum of exponentials

$$S = \sum_i a_i e^{-\alpha_i t}$$

with a power function. In the sum of exponentials

1147735

a_i and α_i are constants and t (the time) is a variable. In our previous reports[41] we showed that the particular case where

$$a_i \propto \alpha_i^{-n}$$

will give rise to a power function where the smallest and largest α's approach zero and infinity, respectively, and all the differences

$$\Delta\alpha_i = \alpha_{i+1} - \alpha_i$$

approach zero as $N \to \infty$. Thus by definition of the Riemann integral

$$\lim_{N \to \infty} \sum_{i=1}^{N} \alpha_i^{-n} e^{-t\alpha_i} \Delta\alpha_i$$

$$\to \int_0^\infty \alpha^{-n} e^{-t\alpha}\, d\alpha = \Gamma(1-n)\, t^{n-1}, \qquad n < 1,$$

where

$$\Gamma(1-n) = \int_0^\infty x^{-n} e^{-x}\, dx .$$

This suggests that the sum,

$$\sum_{i=1}^{N} \alpha_i^{-n} e^{-t\alpha_i}, \qquad (1)$$

might be approximately equal to

$$\frac{1}{\Delta\alpha}\Gamma(1-n)\, t^{n-1}, \qquad n < 1, \qquad (2)$$

over some interval of time not including $t = 0$. Clearly, in Eq. (1) for $t = 0$ and the smallest $\alpha \neq 0$ this function is finite, a property not enjoyed by the function in Eq. (2).

The major reason for undertaking this study is to discover a clue as to why the power function frequently appears to represent data on excretion from and retention in the body when a bone-seeking radionuclide is administered. The power function has been reported by Speckman and Norris,[42] Marshall,[43] Langham *et al.*,[44] Glad *et al.*,[45] and Bernard[46] and others to represent fairly adequately metabolic data.

We present only a brief summary of the results of the studies made using a computer. In the computational work we incremented the α's linearly, that is, we let

$$\alpha_i = \alpha_1 + (i-1)\,\Delta\alpha, \qquad i = 1, 2, \ldots, N, \qquad (3)$$

and we let N range from 10 to 10^4, and $n = -0.5$, 0, 0.333, 0.666, and 0.999. The other two parameters, α_1 and $\Delta\alpha$, took on various values ranging from 10^{-6} to 10^{-2}. Clearly, for the case $n = 0$ one does not need a computer to sum N exponential terms because in that case the sum in (1) under the condition in (3) is a geometric series, and it reduces to the simple expression

$$S = e^{-\alpha_1 t}\, \frac{1 - e^{-N\Delta\alpha t}}{1 - e^{-\Delta\alpha t}} . \qquad (4)$$

For the case $n \neq 0$, no simple expression could be found. In the computations made with the CDC 1604 computer, however, we made computations for $n = 0$ to have a point of reference or of accuracy to check the program. In general we found that as N was increased and $\Delta\alpha$ and α_1 approached zero, the finite sum would more closely approximate the power function in (2) over longer periods of time, but only for the case where $n \leq 0.333$. For $n = 0.666$ or 0.999 the finite sum never did touch the power function as given in (2). Figure 21.19 shows a graph of a typical set of calculations plotted with the Calcomp plotter. Also shown are the power functions which these sums approximate. In this calculation $N = 10^3$, $\alpha_1 = 10^{-6}$, $\Delta\alpha = 2 \times 10^{-6}$, and $n = 0$, 0.333, 0.666, and 0.999. As can be seen, for $n = 0$ and 0.333, the finite sum of terms and the power functions are tangent to one another

[41] *Health Phys. Div. Ann. Progr. Rept. July 31, 1965*, ORNL-3849, p. 201.

[42] T. W. Speckman and W. P. Norris, *Radiation Res.* 23, 461 (1964).

[43] J. H. Marshall, *J. Theoret. Biol.* 6, 386 (1964).

[44] W. H. Langham *et al.*, *Distribution and Excretion of Plutonium Administered Intravenously to Man*, LA-1151 (1950).

[45] B. N. Glad, C. W. Mays, and W. Fisher, *Radiation Res.* 12(6), 672 (1960).

[46] S. R. Bernard, *Health Phys.* 1, 288 (1958).

1147736

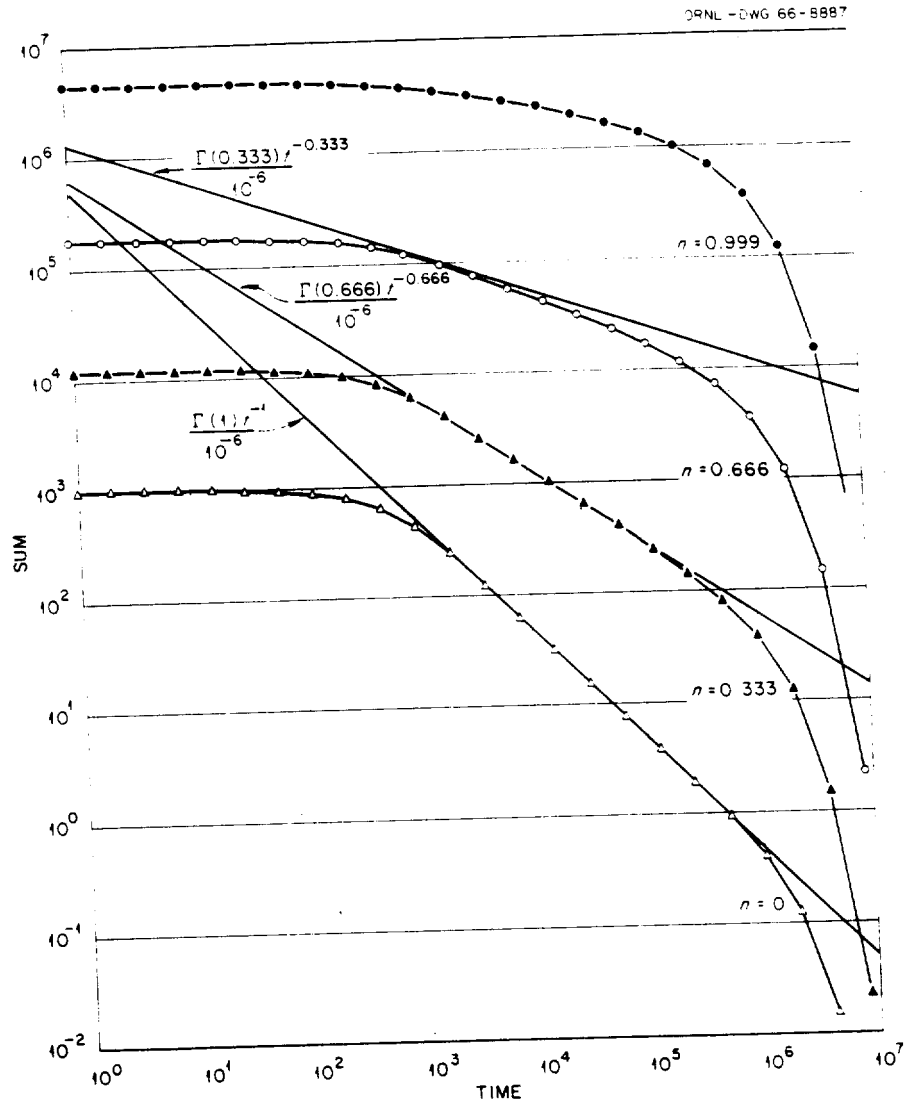

Fig. 21.19. Plot of $\sum_{i=1}^{N} \alpha_i^{-n} e^{-\alpha_i t}$ and $\frac{\Gamma(1-n)}{2 \times 10^{-6}} t^{1-n}$ vs t for $\alpha_i = 10^{-6} + (i-1)\,2 \times 10^{-6}$, $i = 1, 2, \ldots, 1000$, and Various Values of n.

1147737

over at least two decades of time, but for $n = 0.666$ the agreement is not as good over as long a period of time. For the case $n = 0.999$ the power function would be

$$\frac{\Gamma(0.001)\ t^{-0.001}}{10^{-6}} \sim 10^{9} t^{-0.001} ,$$

and the value for $t = 1$ is $\sim 10^{9}$. Note the finite sum at $t = 1$ is $\sim 5 \times 10^{6}$ and differs from the power function by a factor of ~ 200. We observed in all of our computer studies that the agreement between a finite sum and the power function was always poorest where $n = 0.999$. The reasons for this are not known to us.

We also observed that when $(\alpha_1/\Delta\alpha) < \frac{1}{2}$ then an inflection would occur in the log × log graph of the sum vs time and would be more pronounced as $|1 - n|$ increased. Figure 21.20 shows a log × log plot of the sum vs time to illustrate this for $n = -0.5$, 0, 0.333, and 0.999, $\Delta\alpha = 0.01$ and $\alpha_1 = 0.001$. Here $N = 150$ except for the case where $n = -0.5$, in which case $N = 1000$. Note that in all cases except $n = 0.999$ the sum of finite terms intersects the power function twice and undergoes an inflection. It is not difficult to show for the case $n = 0$ that when the condition $(\alpha_1/\Delta\alpha) \geq \frac{1}{2}$ holds, no inflection will occur. No proof for the case $N \neq 0$ has been found yet. However, in our studies we have observed that when $(\alpha_1/\Delta\alpha) \geq \frac{1}{2}$ no inflection occurs in the curves.

We also mention that our work reported here is somewhat similar to that carried out and reported by Turner.[47] He approaches the problem by noting that one might represent the spectrum of the a's and α's in the exponential sum by a continuous function (he chooses a gamma distribution); he then takes the integral over the spectrum of the α's. In his gamma distribution approach, a special form of the power function – one which is finite at the origin – is derived.

[47] M. E. Turner, *Biometrics* 20(4), 827 (1964).

1147738

24. Applied Internal Dosimetry

B. R. Fish

P. E. Brown L. B. Farabee
G. R. Patterson, Jr. R. J. Rawls[1]
J. A. Bains[2]

ORNL IN VIVO GAMMA-RAY SPECTROMETRY FACILITY

P. E. Brown L. B. Farabee
G. R. Patterson, Jr. R. J. Rawls[1]
J. A. Bains[2]

With the beginning of Fiscal Year 1966 the ORNL in vivo counting program entered its fourth phase of operation. The initial phase of developmental operation covered the period June 1960 to July 1961[3] and utilized a 200-channel, tube-type analyzer and a 4 × 4 in. NaI(Tl) crystal. The last six months of this phase included limited routine human counting. The second phase, covering the period July 1961 to November 1962,[4] required additional research and development activities in order to change over to an 8 × 4 in. NaI(Tl) crystal and a transistorized 512-channel analyzer. The third phase, covering the period December 1962 to May 1965,[5,6] was devoted to obtaining base-line counts on essentially everyone with any significant potential for future exposure. The first three phases included slightly more than 4000 human counts. The fourth phase, toward which all the others were directed, is the routine monitoring and evaluation of the extent of exposure to gamma-emitting radioisotopes of all Laboratory employees.

The job of determining which employees should be counted, the frequency with which they should be recounted, and preparing the necessary schedule cards and lists is requiring more time than had been anticipated. The new routine counting program is expected to get under way with the beginning of the new fiscal year. During this interim period, the routine counting of employees has proceeded at a reduced rate; however, several employees thought to have sustained internal exposures have been counted, and other free counting time has been used to advantage in counting standards or performing calibrations needed to evaluate human counts.

During the period from July 1, 1965, through May 31, 1966, a total of 593 counts were made on 463 persons; approximately 89% of the persons counted showed a normal human spectrum on at least one of their counts. In addition to the 593 whole-body counts, 35 counts were made on two persons to determine the location of a contaminant or the amount of activity in a particular organ or part of the body. Table 24.1 summarizes the data for those cases in which measurable amounts of internal radioactivity other than normal ^{40}K and ^{137}Cs were observed. In addition to the human counts a total of 278 calibration and development counts were made; 9

[1]Present address: Hughes Aerospace, Los Angeles, Calif.

[2]Temporary summer employee, Centenary College, Shreveport, La,

[3]B. R. Fish *et al.*, *Health Phys. Div. Ann. Progr. Rept. July 31, 1961*, ORNL-3189, pp. 222–24.

[4]B. R. Fish *et al.*, *Health Phys. Div. Ann. Progr. Rept. July 31, 1962*, ORNL-3347, pp. 147–48.

[5]B. R. Fish *et al.*, *Health Phys. Div. Ann. Progr. Rept. June 30, 1963*, ORNL-3492, pp. 195–205.

[6]B. R. Fish *et al.*, *Health Phys. Div. Ann. Progr. Rept. July 31, 1964*, ORNL-3697, pp. 222–25.

1147739

Table 24.1. Measurable Radioactivity Found in Routine Whole-Body Monitoring Program, July 1, 1965, to May 31, 1966

Isotope	Persons Counted	Maximum Detected (μc)	Percent of MPBB
^{46}Sc	1	0.004	0.008
^{57}Co	2	0.065	0.033
^{60}Co	13	0.012	0.12
^{90}Sr-^{90}Y	4	0.626[a]	43.4
^{95}Zr-^{95}Nb	8	0.039	0.2
^{106}Ru-^{106}Rh	5	0.03	1.0
^{131}I	6	0.006	0.86
^{137}Cs	6[b]	0.092	0.31
^{144}Ce-^{144}Pr	3	0.05	1.0
^{203}Hg	5[c]	0.022	0.55
^{226}Ra	1[d]	<0.0005 μg	0.5
^{235}U	1	Trace possible	
Activity unidentified	7		
Indications of bremsstrahlung	3		

[a]This is the maximum amount detected early in the year for one of two exposure cases which have been followed since January 1964. The average amount for the year was 0.594 μc, which is the equivalent of 39.1% of the permissible lung burden for the equilibrium mixture ^{90}Sr-^{90}Y. The maximum amount of ^{90}Sr detected in persons other than these two known exposures was 0.154 μc, which compared with the MPBB for ^{90}Sr (in equilibrium) is approximately 8% (assuming all in bone).

[b]Radioactive fallout ^{137}Cs is detected in everyone because of assimilation from the diet. The number reported here represents only those who showed 0.045 μc, or roughly three times the average for persons not occupationally exposed.

[c]One person not included in this tabulation was counted following a medical procedure injection of ^{197}Hg. At the time of his first counting, 28 days post injection, the 0.279-Mev peak of ^{203}Hg completely overshadowed the peaks of ^{197}Hg. His whole-body burden of ^{203}Hg at this time was estimated to be 41 μc, or 10.25 times the MPBB.

[d]Three employees of another federal agency installation were counted because of suspected exposure to ^{226}Ra. Only one showed a possibly positive trace of ^{226}Ra.

of these were standards or calibrations for use in the routine human counting program, and 185 of them were counts made to investigate and/or improve counting techniques and capabilities.

IN VIVO DETECTION AND MEASUREMENT OF ^{90}Sr-^{90}Y INTERNAL CONTAMINATION

In January 1964, three laboratory employees were exposed to airborne particulate $^{90}SrTiO_3$.[7,8] The employee who had the smallest indicated deposit originally was, at the time of his last counting, showing <5% of the permissible lung burden; he is no longer being counted frequently. The other two employees are still being counted at approximately one-month intervals using the 8 × 4 in. lead-collimated NaI(Tl) crystal. Figure 24.1 shows the estimated chest burdens for these two employees since their first counts. During this fiscal year their chest counts have averaged approximately 39% of the permissible lung burden for the equilibrium mixture ^{90}Sr-^{90}Y. Judging from the portion of the curves from 180 days post exposure up to 849 days post exposure, it appears that the half-time for lung clearance may be in excess of 1000 days.

COMPUTER ANALYSIS OF WHOLE-BODY COUNT DATA

G. R. Patterson, Jr. E. Schonfeld[9]
M. T. Harkrider[10]

Program WBC,[11,12] written especially for analysis of the ORNL whole-body counting data and in limited use since March 1963, proved to be unsatisfactory from the standpoint of its limited capabilities and its cost of operation. It was capable of evaluating only normal human spectra, or about 75 to 85% of the counts, and required excessive programmer time to correct errors in the program

[7]B. R. Fish *et al.*, *Health Phys. Div. Ann. Progr. Rept. July 31, 1964*, ORNL-3697, pp. 223–24.

[8]B. R. Fish *et al.*, *Health Phys. Div. Ann. Progr. Rept. July 31, 1965*, ORNL-3849, pp. 227–28.

[9]Chemical Technology Division.

[10]Mathematics Division.

[11]B. R. Fish *et al.*, *Health Phys. Div. Ann. Progr. Rept. June 30, 1963*, ORNL-3492, pp. 202–04.

[12]B. R. Fish *et al.*, *Health Phys. Div. Ann. Progr. Rept. July 31, 1964*, ORNL-3697, p. 225.

1147740

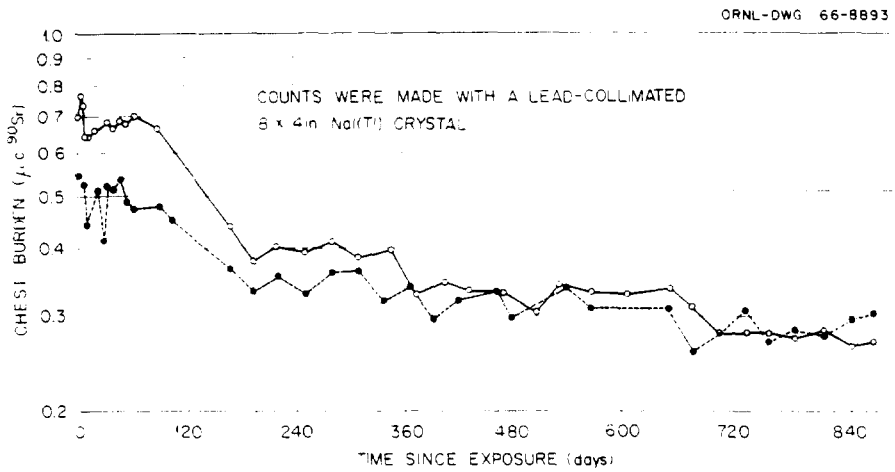

Fig. 24.1. Estimated Lung Burdens of Subjects Inhaling $^{90}SrTiO_3$.

as they became evident. In addition to program deficiencies, we experienced frequent mechanical difficulties in generating punched paper data tapes acceptable by the photoelectric tape reader at the ORNL computing center.

We now have in use a new computer program which can analyze almost any human count we are likely to make and for which we have the necessary calibration standards. An additional advantage is that the new program utilizes punched card data input. The electromechanical equipment used to translate paper data tape to punched cards accepts many tapes which the photoelectric tape reader would not; furthermore, tape errors are easier to spot and correct in the card format.

In July 1965 we evaluated the application to whole-body count data of a new computer program written for the quantitative analysis of the gamma-ray spectra from very low-level radioactive samples. The FORTRAN 63 program ALPHA[13,14] was written by E. Schonfeld of the Chemical Technology Division for analyzing low-level liquid waste samples by least-squares resolution of their gamma-ray spectra. Two test series of routine human counts proved program ALPHA to be directly applicable to whole-body count data analysis without any changes in its original format. The program provides for all the analysis capabilities we desired and is quite flexible. Some of the features of ALPHA which are of particular interest in connection with analysis of in vivo data follow.

1. Evaluation of both normal and abnormal spectra. ALPHA will estimate the amount and standard error of any isotope for which there is a standard in the "library." It will indicate the presence of "suspicious" channels where peaks may exist in the data for which a standard was not available. ALPHA can be instructed to reject a standard and reevaluate the spectrum without reference to that standard if the amount of that activity in the spectrum is less than a prescribed rejection level.

2. The standards "library" has a capacity of up to 80 calibration standards; as many as 20 of these standards can be called for in the analysis of any one "unknown" sample. The "library" can be loaded each time as a punched card deck, or a large "library" can be loaded onto magnetic tape to be used repeatedly.

3. ALPHA can compensate for gain and/or threshold shifts; it can be instructed to match standard and sample peaks automatically or to shift gain and threshold by specified amounts.

4. Both standards and sample data can be input from punched cards or from magnetic tape, or one can be on tape and the other on cards. Spectral data can be in any format as long as the standards and samples are in the same format.

[13] E. Schonfeld, *Alpha — a Computer Program for the Determination of Radioisotopes by the Least-Squares Resolution of the Gamma-Ray Spectra*, ORNL-3810 (July 1965).

[14] E. Schonfeld, A. H. Kibbey, and W. Davis, Jr., *Determination of Nuclide Concentrations in Solutions Containing Low Levels of Radioactivity by Least-Squares Resolution of the Gamma-Ray Spectra*, ORNL-3744 (January 1965).

1147741

```
CARD M=1    20925  1   -0    -0          1  2.000E+01  2.000E+01          -0          -0          -0
                          6356   4430  4501     1 24 66  601  M 12  1812 27 40 36 665 44
     0     88   187   194   231   327   397   357   460   482   561   520   549   583   581
   591    620   558   525   507   472   511   491   420   446   438   447   418   324   343
   336    277   313   306   331   315   220   301   241   245   281   266   179   133   181
   153    151   224   167   168   200   207   219   190   181   219   238   167   180   169
   225    205   215   242   202   149   174   116   138   177   137   150   147   103    75
   104     94    53   149   112   188   224   252   268   282   257   223   221   176   168
   184    211   304   300   452   493   539   539   470   458   342   277   226   163    77
    57     35    42    42    10    22    14    20    22     9    10    23    20    25    39
    11     20    23     6    18    21    45     8    30    34    38    32    15     8    21
    -3      0    44     0     4   -12    38    24    19    20    15    16    47    34     8
   -11     23     5    31    -6    11    14     9    -1     2     7     9    19     7    17
    11      7    15    18    -2     7    33    38    17    17    41    42    60    81    88
    85     74   137   123   123   119   115    76    82    58    66    44    50    37    16
     6     40     8     1    17    10     0    10   -13    10     6    11     3    11    -2
     3    -13     3     2     2    -3    -9     1    -4     1   -11    -8   -11    -1   -21
   -16      3     6   -16     3     0    -3     3   -12     9    -4     7     4    -3     2
   -13    -10    -5    -2    -7     0     2    -1     8    -5     0    -3    -4    -2    -4
    10
BACKGD SUM=    4.100E+04      SAMPLE SUM=    3.196E+04
CARD M=6       3 1=0=0 1     =0=0 1 210
FIT=  1.816E+00 THR SHIFT=  .47 GAIN SHIFT= .9944
FIT=  1.452E+00 THR SHIFT=  .80 GAIN SHIFT= .9907
ALPHA FACTORS
 6.9089E-01  7.0578E-01  8.6832E-01
RESULTS=CONCENTRATIONS AND EST STANDARD ERRORS

                TOTAL-K    1.2729E+02   5.86E+00    137-CS     7.2963E+00   6.10E-01    95-ZR-NB   3.6602E+01   7.37E-01
RATIO OF RESIDUALS OVER STD DEV PER CHANNEL
    -0     -0     -0     -0    1.2    1.8    2.2    1.0     .5    1.1    1.7    2.0    1.5    2.2    2.2
   2.1    2.9    2.6    1.4    1.4     .6     .8    1.2     .1   -.5    -.2    -.2     .2   -1.3   -1.6
   -.9   -1.5    -.8    -.5     .4     .9    -.9     .3    -.3    -.4    1.2    1.0    -.7   -2.1   -1.4
  -1.3   -1.9     .3    -.6   -1.1     .3     .8    1.3     .6     .0    1.5    2.7     .8     .1     .3
   2.3    2.0    2.4    3.4    2.4     .2     .8    -.9    -.3    1.7     .2    1.0    1.3    -.5   -1.9
   -.6    -.9   -2.8    -.1   -1.9    -.4    -.2    -.1     .1     .6    -.3   -1.3   -1.4   -3.3   -4.0
  -4.2   -4.3   -2.4   -3.2    1.1    1.0    2.3    2.3     .9    2.0    -.7    -.5     .0    -.7   -2.2
  -1.8   -1.7    -.3     .2   -1.2    -.4    -.7    -.1    -.4   -1.0    -.5     .2    -.1     .5     .9
   -.9     .0    -.2    -.8     .1     .6    1.3    -.5    1.1    1.3    1.4     .4    -.6    -.7    -.4
  -1.4    -.6     .7   -1.2   -1.6   -1.1    1.0    -.0    -.3    -.3    -.6     .4    1.7     .3   -1.6
  -1.3    -.2    -.2    -.0   -1.3    -.1    -.2    -.9   -1.0    -.6    -.3     .0     .2     .1     .5
   -.2     .3     .5    -.5    -.6    1.0    1.6     .1    -.7     .0     .2     .1     .6     .5    -.5
  -1.4     .1     .6    -.0    -.0    -.1   -1.3   -1.0    -.8    -.3    -.1     .4     .2    -.7    -.9
   1.4     .1    -.8     .7     .5    -.2     .3   -1.2     .1    1.0     .9     .4     .8    -.3     .2
  -1.2    -.2     .2     .2    -.3    -.8    -.2    -.4    -.2   -1.1    -.9   -1.1    -.4   -1.8   -1.8
   -.1     .4   -1.5    -.1     .0    -.3     .2   -1.2     .7    -.5     .6     .7    -.6     .1   -1.9
  -1.3    -.7    -.4   -1.2    -.1     .1     .0    1.1   -1.0    -.2
SUSPICIOUS CHANNELS
 15  16  17  62  63  64
```

Fig. 24.2. Human Body Count Record Sheet – Program ALPHA Printed Output.

114774 2

5. Sample data can be input either as gross counts or net counts. ALPHA corrects both the sample and the background for counting time, adjusts for counter dead time if instructed to, and either subtracts the background or not as instructed.

6. ALPHA can evaluate several counts individually, then combine the results (concentrations and estimated errors) and compute the averages.

Output from program ALPHA is both printed and punched into cards. The printed output, Fig. 24.2, includes all information identifying the sample, estimates of isotope concentrations with standard error, estimates of goodness of fit of standards and samples, the ratio of the residual count over the standard deviation per channel, and indications of which channels may have some activity for which no standard was called from the library. These sheets are filed in chronological order for ready reference to results. The punched card output includes all the identifying information and the estimates of isotope concentration with standard errors. These punched cards can be used in auxiliary programs for plotting of spectra or sorting, tabulating, or compiling data reports, etc. M. T. Harkrider has already written a new program with which we can tabulate weekly or other periodical reports of counting activities using the punched card output deck.

At the present time a library of 86 standards is available on IBM cards; this comprises multiple counts on 20 different isotopes with differing distributions in the calibration phantom or counted in different count configurations. A library of 36 different standards applicable to the latest in vivo counts has been loaded on magnetic tape; this represents multiple counts with differing distributions or different counting configurations of 12 different isotopes. This library, of course, does not include all of the isotopes we may expect to encounter with in vivo counting, and new spectra are being added continually to the library.

CORRECTION OF ^{239}Pu-^{241}Am WOUND COUNT FOR ATTENUATION IN TISSUE AND FOR DIFFERENT RATIOS OF ^{241}Am TO ^{239}Pu

P. E. Brown

There are three main factors that make ^{239}Pu measurement in wounds difficult: (1) the low energy of the photons and the poor yield per disintegration, (2) the varying amounts of ^{241}Am accompanying the ^{239}Pu (this depends on the amount of ^{241}Pu present and age of the source since separation from americium), and (3) the confusion caused by the fact that many of the ^{241}Am photons have almost the same energy as photons from ^{239}Pu.

For counting the low-energy photons a special NaI(Tl) thin-crystal counter, manufactured by Harshaw Chemical Company, Cleveland, Ohio, is used. The background is about 0.5 count/min in the energy bands used, and contribution from gamma rays having energies above 100 kev is very small. The crystal is 1 in. in diameter by $\frac{1}{32}$ in. thick and is covered with a 0.005-in. beryllium window.

Correction for attenuation of these weak photons in the wound tissue can be accomplished approximately by observing the ratio of counts in peaks of different energy. These peaks should be separated as widely as possible. For pure ^{239}Pu the 17- and 53-kev peaks are the only ones that have sufficient difference in energy for this purpose. For ^{241}Am alone the 26- and the 60-kev peaks could be used but are too close in energy to give a good index of attenuation. The 17-to-20-kev band of both ^{239}Pu and ^{241}Am and the 55-to-65-kev band of ^{241}Am have the required difference in energy, but this means that both components must be handled together.

An empirical approach was undertaken by simulating several ^{241}Am/^{239}Pu ratios to represent sources of different ages and different ^{241}Pu content. This was done by the use of a pure ^{239}Pu source (^{241}Am freshly separated) and a pure ^{241}Am source. The two were combined by adding fractional parts of the ^{241}Am and of the pure ^{239}Pu source spectra. A 512-channel Nuclear Data analyzer was used to prepare spectra of counts made with each source separately, using vinyl absorbers ranging from 0.75 to 16 mm thick. Corresponding absorption counts on each source were combined to give five different ^{241}Am/^{239}Pu ratios for each absorber. With these data a graph was prepared to show the thickness of absorber vs the ratio of counts per minute in the 17-kev band to counts per minute in the 60-kev band. Curves for five ^{241}Am/^{239}Pu ratios are shown,

1147743

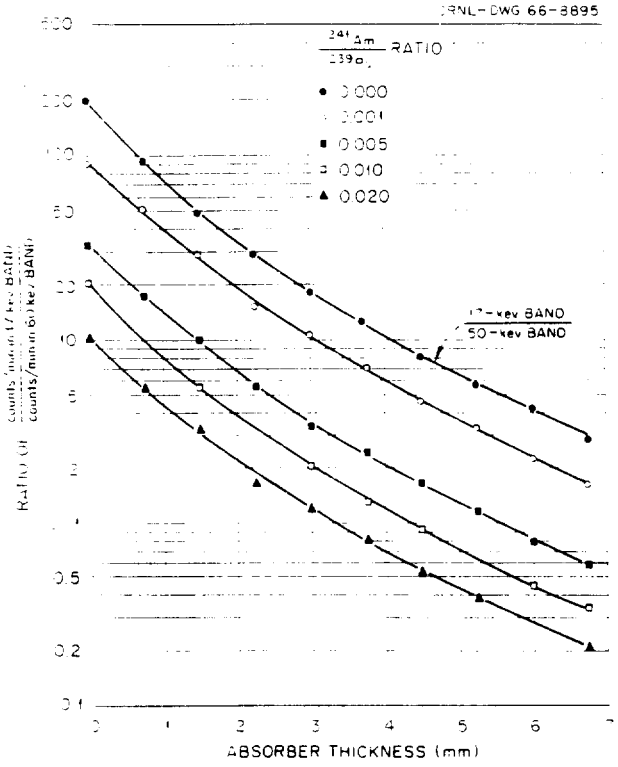

Fig. 24.3. Relative Count Rate in 17- and 60-kev Bands as a Function of Absorber Thickness for Different $^{241}Am/^{239}Pu$ Ratios.

Fig. 24.3. Another graph was prepared showing counting efficiencies for the 17- and 60-kev bands vs thickness of absorber, Fig. 24.4.

It is necessary to know the ratio of ^{241}Am to ^{239}Pu. If such information is not available, it is possible to obtain an estimate using the data given here. A sample of the contaminating material is counted using a few plastic absorbers in the range of those in the graphs. The 17 kev/60 kev counting ratios are plotted in Fig. 24.3, and by comparison of $^{241}Am/^{239}Pu$ ratios already plotted there the proper ratio to use in counting the wound can be estimated. A single count is made in contact with the wound to determine the 17 kev/60 kev counting ratio. Figure 24.4 may then be used to find the counting efficiency. The 17-kev band has the best efficiency for shallow wounds and low $^{241}Am/^{239}Pu$ ratios. The 60-kev band is better for deep wounds and high $^{241}Am/^{239}Pu$ ratios. The least detectable activity (three times the standard deviation of the smallest detectable counting rate) varies with attenuation in tissue and the $^{241}Am/^{239}Pu$ ratio, Fig. 24.5.

The purpose of this investigation was to find a method of correcting ^{239}Pu wound counts for attenuation in tissue and for ratio of ^{241}Am to ^{239}Pu. Additional investigation is under way of the effect of large particle sizes on attenuation. It has not been determined how well the above corrections apply to this problem. Without any such correction an approximately 50% underestimate would occur for 50-μg ^{239}Pu particles in the wound. It is desirable also to know the distribution of activity within the wound, but this procedure gives only the overall or averaged attenuation.

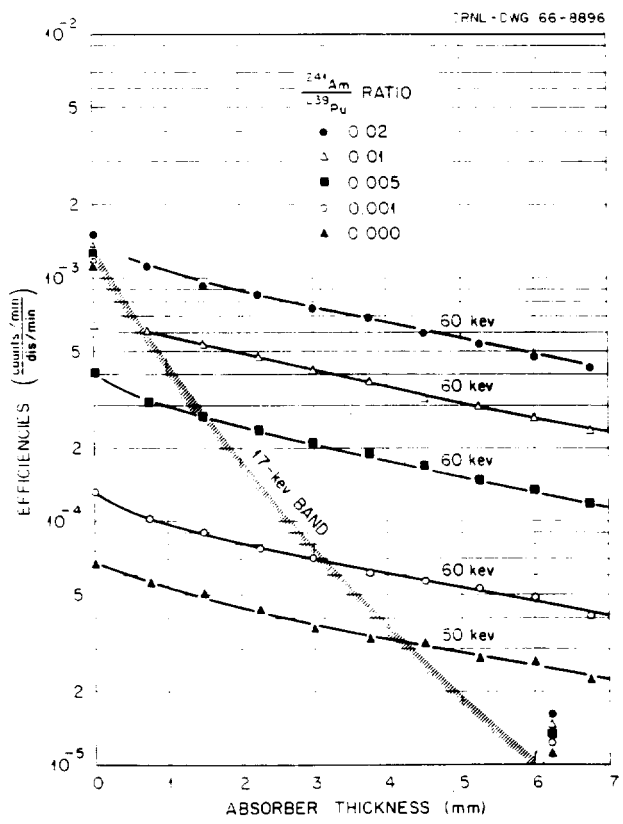

Fig. 24.4. Counting Efficiencies (Counts in Band per Disintegration of ^{239}Pu) vs Absorber Thickness for Different $^{241}Am/^{239}Pu$ Ratios.

1147744

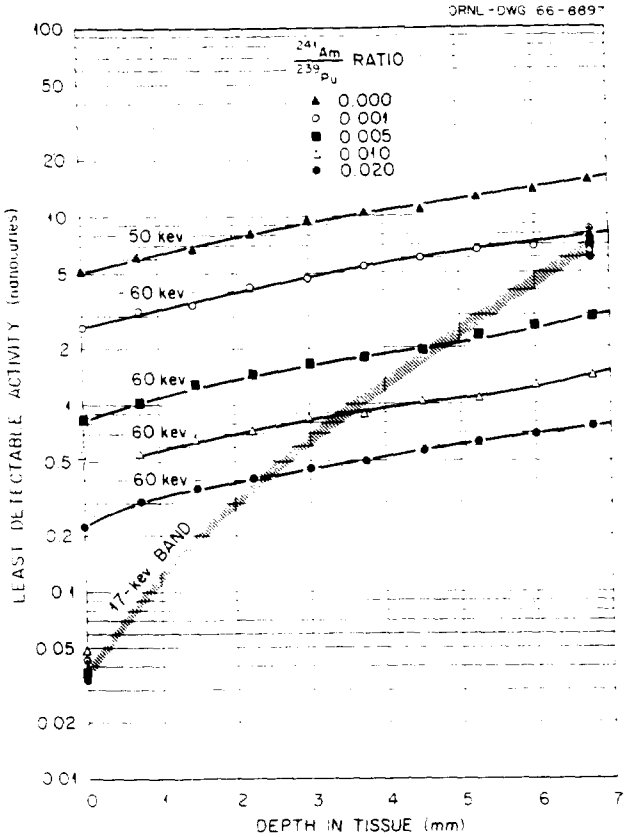

Fig. 24.5. Least Detectable Amount of ^{239}Pu (30-min Count) as a Function of Depth in Tissue for Different $^{241}Am/^{239}Pu$ Ratios.

ABSORPTION OF ^{90}Sr FROM A PUNCTURE WOUND

L. B. Farabee

An employee accidentally received a puncture wound on the volar surface of the tip of the left index finger from a stainless steel wire 1 mm in diameter which was contaminated with ^{90}Sr + ^{90}Y. The absorption of the ^{90}Sr into the body was studied by analysis of blood and urine, while the residual ^{90}Y remaining in the finger was determined by counting the beta activity with an end-window GM beta counter (1.4-mg/cm^2 window).

Although the employee was wearing full protective clothing including four pairs of rubber gloves, the wire pierced the gloves and entered the finger to an estimated depth of about 2 to 3 mm. This depth was estimated by counting the 2.18-Mev beta of ^{90}Y in the finger using layers of polyethylene sheets, and comparing the shape of the absorption curve obtained with that of a known curve derived from a ^{90}Sr-^{90}Y source in a simulated finger counted under similar conditions using the same polyethylene absorbers. The average depth of the ^{90}Y was estimated to be about 1.5 mm. Essentially all of the 0.61-Mev ^{90}Sr was absorbed in the muscle and skin.

In Fig. 24.6 is shown the ^{90}Y content of the finger as determined by the average of four different methods of counting. The ^{90}Y in the first several determinations is abnormally large due to a nonequilibrium condition that existed on the wire. Decontamination of the cell prior to the accident had removed much of the ^{90}Sr, but the ^{90}Y daughter remained on the wire at a level 4.8 times what would have been present in an equilibrium mixture at the time of exposure.

The amount of ^{90}Sr absorbed from the wound was estimated to be 0.051 μc on the basis of a single urine sample collected 4 hr after the incident. And a comparable estimate, 0.073 μc of ^{90}Sr, was obtained from the analysis of a blood sample taken 6 hr after exposure. A urine sample taken five days after the accident indicated an uptake of 0.066 μc. These estimates were obtained by comparison with known human exposures to ^{85}Sr injections.[15]

[15] M. Bishop *et al.*, *Intern. J. Radiation Biol.* 2, 125 (1960).

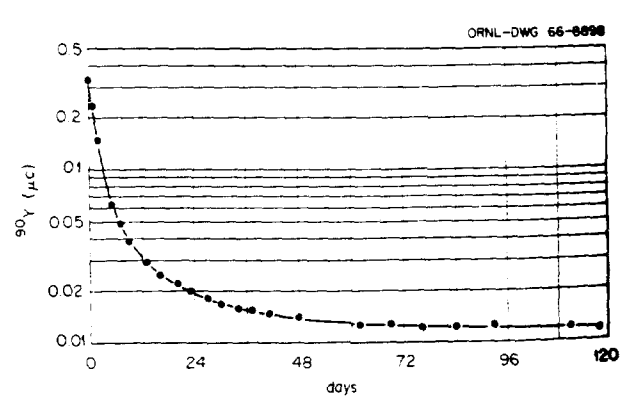

Fig. 24.6. ^{90}Y Content of the Finger as Determined by the Average of Four Different Methods of Counting.

1147745